A study of conceptual model uncertainty in large-scale CO_2 storage simulation

Shuiquan Li,[1] Ye Zhang,[1] and Xu Zhang[2]

[1]   In this study, multiscale permeability upscaling is combined with a sensitivity study of model boundary condition to identify an optimal heterogeneity resolution in developing a reservoir model to represent a deep saline aquifer in CO_2 storage simulation. A three-dimensional, fully heterogeneous reservoir model is built for a deep saline aquifer in western Wyoming, where each grid cell is identified by multiple material tags. On the basis of these tags, permeability upscaling is conducted to create three increasingly simpler site models, a facies model, a layered model, and a formation model. Accuracy of upscaling is evaluated first, before CO_2 simulation is conducted in all models. Since at the injection site, uncertainty exists in the nature of the reservoir compartment, end-member boundary conditions are evaluated, whereby brine production is introduced to control formation fluid pressure. The effect of conceptual model uncertainty on model prediction is then assessed for each boundary condition. Results suggest that for the spatial and temporal scales considered, without brine production, optimal complexity of the upscaled model depends on the prediction metric of interest; the facies model is the most accurate for capturing plume shape, fluid pressure, and CO_2 mass profiles, while the formation model is adequate for pressure prediction. The layered model is not accurate for predicting most of the performance metrics. Moreover, boundary condition impacts fluid pressure and the amount of CO_2 that can be injected. For the boundary conditions tested, brine production can modulate fluid pressure, affect the direction of mobile gas flow, and influence the accuracy of the upscaled models. In particular, the importance of detailed geologic resolution is weakened when viscous force is strengthened in relation to gravity force. When brine production is active, variability of the predictions by the upscaled models becomes smaller and the predictions are more accurate, suggesting a subtle but important interplay between heterogeneity resolution, fluid driving forces, and model predictions.

Citation: Li, S., Y. Zhang, and X. Zhang (2011), A study of conceptual model uncertainty in large-scale CO_2 storage simulation, *Water Resour. Res.*, *47*, W05534, doi:10.1029/2010WR009707.

1.   Introduction

[2]   Carbon dioxide (CO_2) is believed to be a driving force behind recent observations of global climate change. To reduce the amount of CO_2 entering the atmosphere, a variety of actions are proposed, including CO_2 capture from industrial sources and subsequent storage into deep, permeable geologic formations (carbon capture and storage, or CCS) [*Intergovernmental Panel on Climate Change* (*IPCC*), 2005]. Candidates for such formations include unminable coal seams, depleted oil and gas reservoirs, and deep saline aquifers. The last category, ubiquitous in the world's sedimentary basins and easily accessible from CO_2 point sources, constitutes up to 90% of the total geostorage volume. Deep saline aquifers are thus considered ideal for CO_2 storage in both onshore and offshore settings [*Orr*, 2009], particularly for commercial-scale operations.

[3]   In deep aquifers, CO_2 exists in a supercritical "gas" phase that is less dense than formation brine. Under the imposed pressure gradient from injection, it will spread out laterally as well as rise and flow toward the caprock under buoyancy, dissolving into brine as it migrates. Along the trailing plume, a portion of the CO_2 can become trapped due to the imbibition of brine and associated CO_2 relative permeability hysteresis [*Flett et al.*, 2004]. Thus during and after injection, dissolved, trapped, and mobile CO_2 can all exist in a storage formation. Over longer times, dissolved CO_2 can react with the formation rock matrix, creating mineral precipitates, or dissolution, or both, though fluid-rock reactions are considered slow in quartz-dominated sandstones [*IPCC*, 2005]. Currently, a variety of ongoing and planned saline aquifer storage projects exist [*Michael et al.*, 2009a, 2009b], including both pilot-scale and larger operations. At these sites, while CO_2 storage is demonstrated to be technically feasible, several issues must be considered before commercial-scale injection can become a reality.

[4]   First, commercial-scale injection requires a storage capacity that is orders of magnitude larger than those cur-

[1]Department of Geology and Geophysics, University of Wyoming, Laramie, Wyoming, USA.
[2]Schlumberger Information Solutions, Schlumberger, Houston, Texas, USA.

rently assessed by the existing operations [*Michael et al.*, 2010]. At such scales, to quantify CO_2 flow and storage and to predict its footprint following injection and closure, deep saline aquifers need to be characterized at the regional scale and, accordingly, large-scale geologic site models must be built. However, unlike hydrocarbon reservoirs which can be characterized with site laboratory or field data, deep saline aquifers often suffer from extreme data scarcity. Using standard geophysical and borehole techniques to characterize them will make the storage project prohibitively expensive. For example, the cost of a seismic survey increases greatly with lateral extent of the survey, depth of investigation, and resolution desired to map the storage system. Borehole sampling, which can provide downhole petrophysical properties of the aquifer, e.g., porosity (ϕ) and permeability (k), needs to be minimized to reduce cost and leakage risk [*Carey et al.*, 2007]. Owing to these limitations, most saline aquifers are not extensively characterized, and accordingly, CO_2 modeling carried out as part of a site assessment study employs a variety of assumptions to simplify the construct of the site model. In particular, depending on the quality and accessibility of site-specific data, subsurface environment is commonly parameterized assuming permeability homogeneity at various scales.

[5] For example, to predict basin-scale CO_2 storage capacity and plume footprint in response to a hypothetical injection scenario in the Illinois Basin, the target saline aquifer is modeled at the scale of a geological formation [*Birkholzer and Zhou*, 2009; *Zhou et al.*, 2010]. At such scales, field or laboratory data are often limited, and homogeneous properties are assigned to the model units [e.g., *Law and Bachu*, 1996; *McPherson and Cole*, 2000; *Maldal and Tappel*, 2004; *Pruess et al.*, 2004; *Nordbotten et al.*, 2005; *Hesse et al.*, 2006; *Sasaki et al.*, 2008; *Stauffer et al.*, 2009]. On the other hand, where more data are available, within-aquifer heterogeneity has been modeled as distinct facies [*Johnson et al.*, 2001; *Hollowway et al.*, 2004; *Obi and Blunt*, 2006; *Primera et al.*, 2009]. These units can include interconnected high permeability (high-k) channels embedded in low permeability (low-k) clay, or reversely, low-k clay or shale lenses embedded in sand or, in the case of *Doughty and Pruess* [2004], multiple facies with variable mean ϕ and k. By explicitly modeling facies distribution, effect of facies-controlled heterogeneity on CO_2 flow and storage can be quantified. Furthermore, approaches other than facies modeling have also been adopted. For example, *Kumar et al.* [2004] divided an aquifer into many layers, with each layer assuming a different permeability. Geostatistics-based heterogeneity has been investigated, which describes either random or semistructural distribution of permeability within aquifers [*Flett et al.*, 2007; *Ide et al.*, 2007; *Qi et al.*, 2007]. Simulation results further suggest that models incorporating high-resolution heterogeneity are needed to accurately assess the various storage schemes [*Juanes et al.*, 2006; *Qi et al.*, 2009]. This view is echoed by petroleum researchers who stated that the capture of small-scale reservoir geometry down to the scales of bedding planes can improve model estimates of hydrocarbon recovery [*Elfenbein et al.*, 2005].

[6] In CO_2 modeling, a variety of approaches have thus been used to capture heterogeneity in a storage aquifer, some resolving heterogeneity down to fine scales, while others use simple configurations assuming homogeneity. These approaches have rarely been compared among one another to identify which one might be optimal for CO_2 modeling. Here, the word "optimal" is used rather than "accurate" since it is widely acknowledged that a better resolution of subsurface heterogeneity will lead to more accurate predictions of fluid flow and transport. For example, in the work of *Zhang et al.* [2006], we demonstrated that a facies model of higher geologic resolution is more accurate than a formation model in predicting groundwater flow. In the work of *Zhang and Gable* [2008], we further demonstrated that although some aspects of transport modeling (e.g., plume centroid and covariance) can be captured by the facies model, other aspects (e.g., plume breakthrough and tailing) require detailed heterogeneity. In CO_2 modeling, however, particularly in assessing the problem of large-scale storage in regional aquifers, detailed description of heterogeneity in three dimensions down to the smallest resolvable continuum scale (e.g., core measurements) is likely unobtainable. Thus a relevant question is not whether finer heterogeneity resolution should lead to more accurate predictions (we believe that the answer to this question is yes) but whether we can identify a level of heterogeneity resolution in a geological storage model that is sufficiently accurate in predicting a variety of CO_2 performance metrics.

[7] The issue of optimal heterogeneity resolution is being explored by petroleum researchers concerned with reservoir production in extremely data-poor environments [e.g., *Castellini et al.*, 2003; *Friedmann et al.*, 2003]. Using a set of characterization data for a deepwater reservoir, *Milliken et al.* [2007] built two families of geologic models at different complexities. The same oil production scenario was simulated to determine if the simpler models (e.g., a formation model consisting of a series of stacked channels) could be used to predict the behaviors of the more complex models (e.g., each channel in the formation incorporates five facies, where each facies is characterized with a different ϕ and k distribution). The goal is to identify an optimally simple model for flow predictions, since the cost of building the complex models is extremely high. However, though the simpler models were identified to provide aspects of predictions similar to those of the complex models, the two families of models are not strictly comparable, i.e., they do not provide the same bulk flow predictions under the same production scenarios.

[8] Besides the uncertainty in developing a site conceptual model for CO_2 simulation, another issue that is relevant for the success of large-scale storage is injectivity [*Stauffer et al.*, 2009; *Michael et al.*, 2010]. As commercial-scale injection proceeds, a large volume of brine can be displaced from the injection site. In a deeply buried aquifer, without an outlet to dispose of the brine, formation fluid pressure can build up, creating a footprint that can extend to regional scales [*Zhou et al.*, 2008; *Birkholzer et al.*, 2009]. Though bottomhole pressure (BHP) constraint can be set to shut down the injector, little CO_2 can in turn be injected, severely limiting injectivity. Without this constraint, however, damaging fluid pressure buildup can potentially fracture the formation and its caprocks, creating leakage pathways. Neither option is acceptable for commercial-scale storage of CO_2 in saline aquifers. During injection, a set of measures must be taken to address pressure buildup and brine displacement while ensuring injectivity. These measures should also take into account site boundary characteristics, i.e., whether the reservoir is compartmentalized or not. Without appropriate well tests, this

information also suffers uncertainty. To date, most proposed strategies to address pressure buildup are based on brine production [Flett et al., 2008; Qi et al., 2009; Surdam et al., 2009; Wolery et al., 2009]. However, they have not been evaluated within the context of alternative conceptual models and uncertain site boundary condition. Will a brine production strategy developed assuming formation homogeneity still be effective if the underlying heterogeneity is revealed? And, is the boundary condition and its uncertainty important to flow prediction? These questions are difficult to assess without prior information on reservoir heterogeneity.

[9] In this study, multiscale permeability upscaling is combined with a sensitivity study of model boundary condition to identify an optimal model complexity in developing a reservoir model for CO_2 storage simulation. Unlike past research where models of various complexities were developed at different sites, a suite of reservoir models, each of a different complexity, is developed for the same site. The simpler models are created based on an underlying and (assumed) fully known heterogeneous reservoir model (FHRM), which serves as a reference for predictions. To create a consistent framework for model comparison, permeability upscaling is used to link the simple models to the FHRM. CO_2 injection is then simulated in all models. By comparing a suite of prediction metrics against that of the FHRM, our goal is to identify a simple model that is sufficiently accurate for predicting gas migration, CO_2 storage, and pressure buildup, thus contributing to the development of a cost-effective strategy in developing site models for CO_2 simulations. The methodology presented is general and can be applied to any storage site. It is tested here on a reservoir model developed for a proposed commercial-scale injection site in western Wyoming.

[10] In the remainder of the article, the upscaling method is introduced first, followed by a description of the reservoir models. A sensitivity study is presented, including simulation technique, parameters used, and injection design. Results illustrate the impact of both conceptual model uncertainty and boundary condition on CO_2 flow and storage predictions. Findings of the study are discussed and summarized before directions for future research are indicated.

2. Method

2.1. Permeability Upscaling

[11] To assess the effect of heterogeneity resolution on CO_2 prediction, besides a FHRM, a set of simple (or upscaled) models can be created under different simplifying assumptions, e.g., a formation that is homogeneous, one exhibiting multiple facies, or one consisting of multiple layers. To facilitate model comparison, an upscaling analysis is used so that the simple models become equivalent to the FHRM in flow prediction. In the following sections, both intrinsic and relative permeability upscaling are discussed.

[12] In intrinsic permeability upscaling, equivalent permeability ($k*$) can be computed based on results of single-phase steady state flow modeling in the FHRM. $k*$ is assigned to each unit of the upscaled models to represent the effect of unresolved, subunit permeability heterogeneity on single-phase predictions. Since in developing a site model for CO_2 storage, the model units can be irregular, this upscaling is accomplished using a numerical technique described by Zhang et al. [2006], where a 2-D system was first analyzed. Herein, the earlier formulation is extended to 3-D, with a few modifications:

$$
\begin{bmatrix}
\langle\frac{\partial\Phi}{\partial x}\rangle_1 & \langle\frac{\partial\Phi}{\partial y}\rangle_1 & \langle\frac{\partial\Phi}{\partial z}\rangle_1 & 0 & 0 & 0 & 0 & 0 & 0 \\
0 & 0 & 0 & \langle\frac{\partial\Phi}{\partial x}\rangle_1 & \langle\frac{\partial\Phi}{\partial y}\rangle_1 & \langle\frac{\partial\Phi}{\partial z}\rangle_1 & 0 & 0 & 0 \\
0 & 0 & 0 & 0 & 0 & 0 & \langle\frac{\partial\Phi}{\partial x}\rangle_1 & \langle\frac{\partial\Phi}{\partial y}\rangle_1 & \langle\frac{\partial\Phi}{\partial z}\rangle_1 \\
\langle\frac{\partial\Phi}{\partial x}\rangle_2 & \langle\frac{\partial\Phi}{\partial y}\rangle_2 & \langle\frac{\partial\Phi}{\partial z}\rangle_2 & 0 & 0 & 0 & 0 & 0 & 0 \\
0 & 0 & 0 & \langle\frac{\partial\Phi}{\partial x}\rangle_2 & \langle\frac{\partial\Phi}{\partial y}\rangle_2 & \langle\frac{\partial\Phi}{\partial z}\rangle_2 & 0 & 0 & 0 \\
0 & 0 & 0 & 0 & 0 & 0 & \langle\frac{\partial\Phi}{\partial x}\rangle_2 & \langle\frac{\partial\Phi}{\partial y}\rangle_2 & \langle\frac{\partial\Phi}{\partial z}\rangle_2 \\
\ldots & \ldots & \ldots & \ldots & \ldots & \ldots & \ldots & \ldots & \ldots \\
\langle\frac{\partial\Phi}{\partial x}\rangle_m & \langle\frac{\partial\Phi}{\partial y}\rangle_m & \langle\frac{\partial\Phi}{\partial z}\rangle_m & 0 & 0 & 0 & 0 & 0 & 0 \\
0 & 0 & 0 & \langle\frac{\partial\Phi}{\partial x}\rangle_m & \langle\frac{\partial\Phi}{\partial y}\rangle_m & \langle\frac{\partial\Phi}{\partial z}\rangle_m & 0 & 0 & 0 \\
0 & 0 & 0 & 0 & 0 & 0 & \langle\frac{\partial\Phi}{\partial x}\rangle_m & \langle\frac{\partial\Phi}{\partial y}\rangle_m & \langle\frac{\partial\Phi}{\partial z}\rangle_m \\
0 & 1 & 0 & -1 & 0 & 0 & 0 & 0 & 0 \\
0 & 0 & 1 & 0 & 0 & 0 & -1 & 0 & 0 \\
0 & 1 & 0 & 0 & 0 & 1 & 0 & -1 & 0
\end{bmatrix}
\cdot
\begin{Bmatrix}
k_{xx} \\ k_{xy} \\ k_{xz} \\ k_{yx} \\ k_{yy} \\ k_{yz} \\ k_{zx} \\ k_{zy} \\ k_{zz}
\end{Bmatrix}
= (-\mu)
\begin{Bmatrix}
\langle q_x\rangle_1 \\ \langle q_y\rangle_1 \\ \langle q_z\rangle_1 \\ \langle q_x\rangle_2 \\ \langle q_y\rangle_2 \\ \langle q_z\rangle_2 \\ \ldots \\ \langle q_x\rangle_m \\ \langle q_y\rangle_m \\ \langle q_z\rangle_m \\ 0 \\ 0 \\ 0
\end{Bmatrix}
\tag{1}
$$

Table 1. Symbols and Units of This Study[a]

Parameter	Unit	Symbol
Porosity	fraction	ϕ
Permeability	mdarcy	k
Natural log permeability	mdarcy	$\ln k$
Log permeability	mdarcy	$\log k$
Horizontal permeability	mdarcy	k_H
Vertical permeability	mdarcy	k_V
Pressure	Psia	P
Temperature	°F	T
Phase saturation	fraction	S_i
Concentration of CO_2 in brine	ppm	C_i
Residual water saturation	fraction	S_w^{res}
Critical gas saturation	fraction	S_g^c
Residual gas saturation	fraction	S_g^{res}
Water endpoint relative permeability	fraction	k_{rw}^{end}
Gas endpoint relative permeability	fraction	k_{rg}^{end}
Injection rate	Mscf/d	r_i
Production rate	Mscf/d	r_p
Pore volume	cf	V_p
Component mass	lb mol or Mt	-
Phase Density	lb/ft^3	ρ_i
Phase Viscosity	cP	μ_i
Fluid Potential	Psi	Φ
Fluid potential gradient	Psi/ft	$\nabla\Phi$
Aquifer influx rate	stb/d	QR

[a]Mscf/d is 1000 standard cubic feet per day; lb mol is pound mole; Mt is one million metric ton; stb/d is standard barrel per day.

where $\langle\ \rangle$ represents spatial averaging among grid cells that belong to the same upscaling unit; q_x, q_y, q_z are components of the single-phase Darcy flux; Φ is fluid potential (water is the fluid chosen for upscaling, thus $\Phi = \rho g h$, h is hydraulic head); ρ and μ are fluid density and dynamic viscosity, respectively; subscripts 1, 2, …, m denote flow experiments conducted using the FHRM, driven by distinct boundary conditions (m is ideally a large number, subjecting the model to many flow stimulations); k_{xx}, …, k_{zz} are components of the upscaled $\mathbf{k}^*$ (symbols and units are listed in Table 1). For each unit of the upscaled models, equation (1) must be assembled and solved once. More details on how equation (1) is assembled from multiple flow experiments can be found in the work of *Zhang et al.* [2006]. For 3-D upscaling, a few points need to be elucidated.

[13] First, the total number of flow experiments m must be ≥ 3 to obtain a unique solution. As discussed by *Zhang et al.* [2006], when the upscaling domain size is larger than the underlying $\ln(k)$ correlation ranges, $\mathbf{k}^*$ becomes insensitive to the number of m used and the associated flow patterns. To obtain $\mathbf{k}^*$, fewer flow experiments can thus be theoretically carried out (in that 2-D study, both linear and nonlinear flow patterns were tested for $m = 2$ and $m = 4$, respectively). Whether this is still true in 3-D will be tested here as well.

[14] Second, the last three equations of equation (1) are constraints added to ensure symmetry in $\mathbf{k}^*$. Depending on the magnitude of the gradient terms in the coefficient matrix, these equations may need to be rescaled to reduce numerical truncation error and to ensure a stable inversion. However, the enforcement of symmetry does not guarantee the creation of a positive definite $\mathbf{k}^*$, which is required for modeling physically correct flow by the upscaled models. (In 2-D experiments with images exhibiting truncated heterogeneity, 1~2% of the upscaled $\mathbf{k}^*$ was found to be non-positive-definite.) In this study, equivalent $\mathbf{k}^*$ is tested for positive-definiteness before being assigned to the upscaled models.

[15] Third, the numerical technique implemented in equation (1) can be considered as a global method within the context of single-phase upscaling (see reviews [e.g., *Wen and Gomez-Hernandez*, 1996; *Renard and de Marsily*, 1997; *Sanchez-Vila et al.*, 2006]). That is, $\mathbf{k}^*$ of any unit of the upscaled models is calculated using averages of potential gradients and fluxes which are computed from global flow simulations that extend beyond the particular unit. It differs from the local-based methods in that upscaling is concerned with a model region (e.g., a facies unit) instead of seeking coarse-grid parameters from fine-grid k distributions. The later is used in coarse-graining research for the specific goal of achieving higher computation efficiency in fluid flow modeling. Though an important topic on its own (e.g., the global method is invariably more expensive than the local methods, whether the upscaling concerns model regions or coarsened grids), this topic is not pursued here. The FHRM and the upscaled models share the same grid and are considered alternative conceptual models; thus numerical discretization error does not come into play in model comparison. Nevertheless, it is useful to point out that global methods can be more accurate than local methods, since flow channeling due to permeability correlation outside the upscaling domain can be accounted for in calculating $\mathbf{k}^*$. This is confirmed by observations that the accuracy of a local method increases when the size of the upscaling block surrounding the grid cell increases [*Wen et al.*, 2003]. Given advances in computing techniques, limitation of the global method may be overcome in time and its strength better realized in the future. In this study, the technique is used to help establish single-phase flow equivalence among various model representations.

[16] The implementation of equation (1), however, is not straightforward with reservoir models employing irregular grids (i.e., grid lines nonorthogonal to one another nor aligned with the simulation axes). The FHRM is built with a commercial package (Petrel, 2009, available at http://www.slb.com/services/software/geo/petrel.aspx), resulting in an irregular corner point grid. The flow simulation is done using Eclipse 300 [*Schlumberger*, 2009], an integrated finite difference (FD) simulator that interfaces with this grid. CO_2 storage is modeled with the GASWAT module of Eclipse 300. A single simulation platform is thus used in permeability upscaling, its verification, and CO_2 modeling. However, Eclipse does not export fluid potential gradient, only potential at the centroid of the grid cells. Owing to the irregular grid, the gradient cannot be computed directly with finite difference. A postprocessing program is thus written which converts the corner point grid to a finite element (FE) grid. This program is verified by conducting permeability upscaling for a 3-D synthetic aquifer with an orthogonal grid [*Zhang et al.*, 2011]. Finite difference is used to compute the gradient, which is compared to that computed with the FE program. Results are consistent when multiple variances are tested. In this study, each grid cell contains eight corner points; thus the FE formulation is based on eight-node cells and linear shape functions. Since Eclipse is a general-purpose transient simulator, a special module is required to drive steady state flow through the model, which is needed for $\mathbf{k}^*$ upscaling and its verification. Detailed information on how this module is set up is described elsewhere [*Zhang et al.*, 2011].

[17] Besides intrinsic permeability upscaling, effective relative permeability functions (one for CO_2 and one for brine) can be obtained using results of two-phase flow modeling in the FHRM [*Ertekin et al.*, 2001]. This approach is referred to as dynamic upscaling, and if the grid is simultaneously coarsened, the upscaled relative permeability functions are referred to as pseudofunctions. Here, since all models share the same grid, only the effective relative permeability functions are of relevance. The effective functions can be adjusted from those of the local functions (or "rock curves") assigned to the FHRM, i.e., those assigned to individual grid cells that belong to different relative permeability families, which is typically controlled by and measured for individual facies in the reservoir. In upscaling for relative permeabilities, the goal is to ensure that the upscaled models predict the same flow rate for each fluid phase, similar to single-phase flow equivalence in intrinsic permeability upscaling. The effective functions are generally a tensor property that can vary with flow rate (e.g., viscous- versus capillary-dominated, viscous- versus gravity-dominated, etc.), flow direction, and boundary condition [*Ataie-Ashtiani et al.*, 2002; *Pickup et al.*, 2005; *Braun et al.*, 2005]. Studies have shown that if the upscaling domain is large compared to $\ln(k)$ correlation range, and if the rock curves are uniform in the reservoir, and if capillary pressure effect is negligible, the effective relative permeability of upscaled models may be approximated by the local (and uniform) rock curves of the heterogeneous model [*Sáez et al.*, 1989; *Amaziane et al.*, 1991; *Das et al.*, 2004]. The first criterion is satisfied in this study (discussed later). To simplify the analysis, the same relative permeability functions are assigned to the grid cells of the FHRM, disregarding potential differences among grid cells belonging to different facies (i.e., intrinsic permeability groups). In CO_2 modeling, capillarity is also ignored. Therefore the upscaled models employ the same relative permeability functions as those of the FHRM.

2.2. Model Creation

[18] The FHRM and its equivalent, upscaled models are created based on a reservoir model developed for a deep saline aquifer in western Wyoming (Nugget Sandstone), a proposed commercial-scale CO_2 storage formation. The reservoir model is heterogeneous with 134,064 grid cells (Figure 1). It was first upscaled using a local method from a 3-million-cell geostatistical grid which has a laterally isotropic permeability with a vertical-to-lateral anisotropy ratio of 0.2 [*Li et al.*, 2011]. Diagonal upscaling was used [*Li et al.*, 2011]; thus local permeability of the FHRM is a diagonal tensor. The geostatistical model was built with a hierarchical approach, integrating structural, facies, and petrophysical data. Upon grid coarsening to create the FHRM, the (fine-grid) facies types were conformably mapped onto the coarse model. Thus each cell of the FHRM is labeled with a facies tag. Using these tags, a four-unit facies model is created for this study (Figure 1).

[19] In building reservoir models with sparse data, facies can be "picked" from wireline logs. Using these picks, layered models are created assuming lateral continuity away from well control. At other times, layers may be created by simple division of the reservoir thickness. In this study, a three-unit layered model is created based on the observed variability in the FHRM (Figure 1). The upper zone, being twice as thick as the lower zone, is divided into two layers. The lower zone, despite its variable heterogeneity, is not subdivided because (1) heterogeneity in this zone is irregular and is not structured as layers and (2) we wish to examine the consequences of using simple layers while ignoring underlying variability. Finally, a formation model is created representing the reservoir with one unit (Figure 1).

[20] The creation of simple models using the above divisions is nonunique, as alternative approaches for labeling stratifications exist, e.g., based on percolation cluster or connectivity analysis. The divisions adopted here reflect approaches in CO_2 modeling in data-poor settings, as summarized in section 1. The number of units in the upscaled models is used as a proxy for model complexity, since data requirement and associated cost of building the model will likely increase with the level of heterogeneity resolution. For example, the FHRM is considered the most complex and expensive to build, followed by the facies model (less expensive, since potentially petrophysical properties of the facies can be borrowed from analog data [*Milliken et al.*, 2007]), which is followed by the layered model (e.g., thickness-based division), and the formation model. Note, however, to develop insights into model complexity, this study is conceptual, whereby the FHRM provides a basis to create the simpler models. For a real reservoir, if data availability is such that a FHRM can be developed, simpler models would not likely be created from its homogenization because one would generally prefer to build as detailed a model as the underlying data allow. The simple models here are hypothetical; only if no data exist to create detailed heterogeneity in the first place, these models would be used. They are meant to represent alternative models created due to lack of data.

[21] For each simple model, frequency distribution of the underlying, within-unit horizontal permeability (k_x) is shown (Figure 2). For the formation model, k_x varies over 5 orders of magnitude. Its histogram is multimodal with a $\ln(k)$ variance of 3.2, reflecting heterogeneity of the entire reservoir. A significant volume fraction occurs near the median permeability of 21 mdarcy, corresponding to the thick and more uniformly distributed upper reservoir (Figure 1). For the facies model, since ϕ was separately modeled for each facies unit using Sequential Gaussian Simulation and $\log(k_x)$ was mapped from ϕ [*Li et al.*, 2011], permeability histograms of the facies units are approximately unimodal with lognormal distributions. These histograms correspond to the individual modes in the histogram of the formation model, as expected. For the layered model, the upper two units have unimodal distributions occurring near the median permeability, while the bottom unit has a bimodel distribution spreading over the full range of variability. In the lower reservoir, visual inspection reveals a sheetlike high-k structure in the southern region (Figure 1), with preferential continuity along the N-S direction. This continuity, embedded in low-k deposit, is captured by the facies model (unit 4) but not by the layered model. The frequency distribution of the within-unit vertical permeability has similar characteristics as those described for k_x and will thus not be presented.

2.3. CO_2 Simulation

[22] CO_2 simulation is conducted with GASWAT (2009 version) [*Schlumberger*, 2009], a multiphase compositional
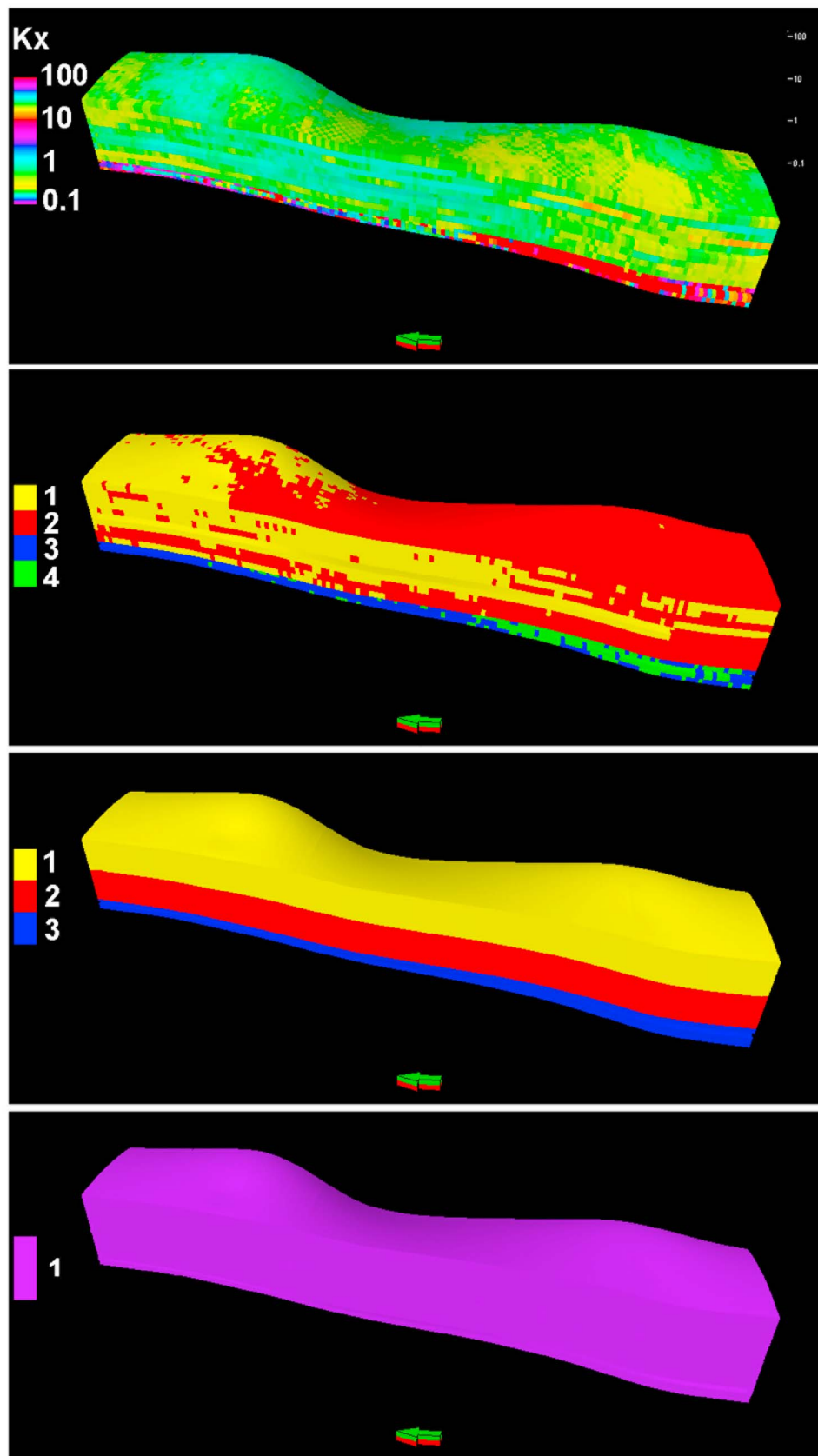
Figure 1. Reservoir models evaluated in this study. From top to bottom are shown FHRM (horizontal permeability in mdarcy), four-unit facies model (facies IDs are shown), three-unit layered model (layer IDs are shown), and a formation model. All models employ 15 times vertical exaggeration. Arrow points north.
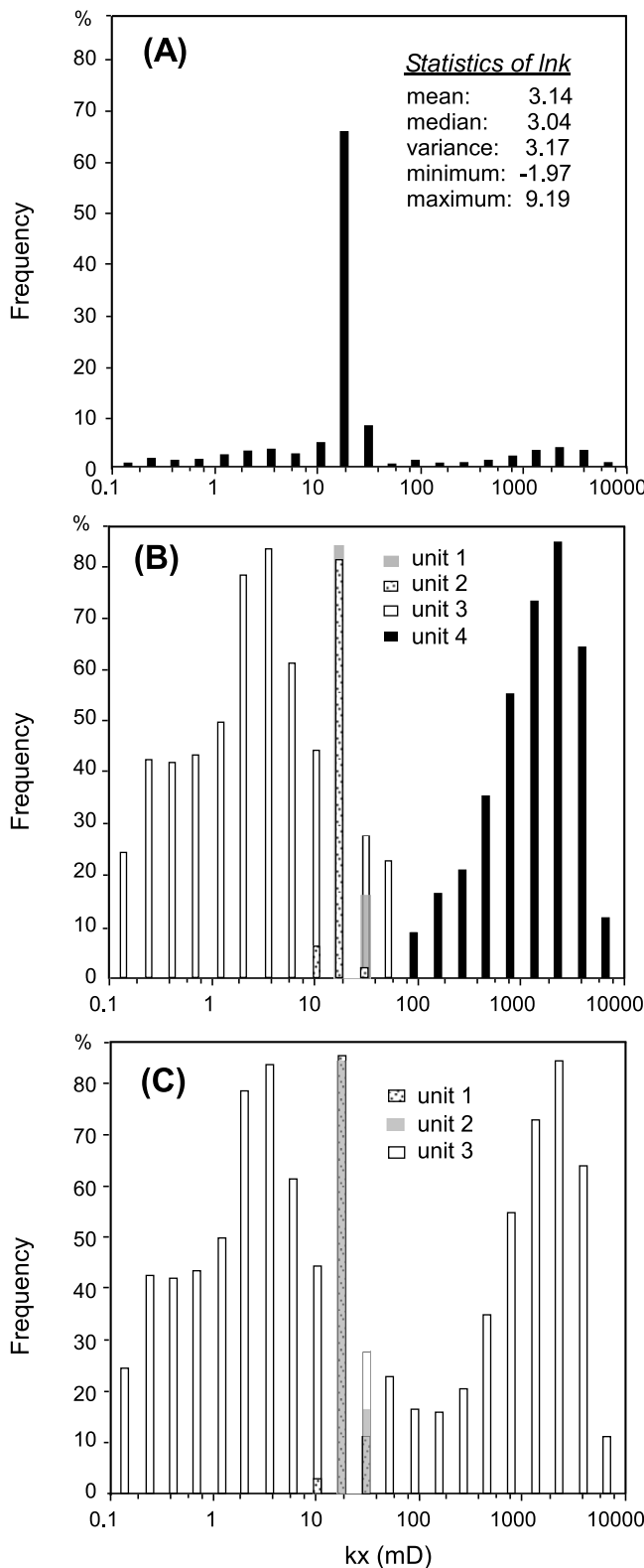
Figure 2. Histograms of within-unit horizontal permeability (k_x, x is oriented east-west): (a) formation model; (b) facies model; (c) layered model. Permeability is shown in log scale; tick marks within one log cycle (e.g., 10 to 100) represent 20, 40, 60, and 80 mdarcy. For the facies and layered models, histograms of the individual units are superimposed into the same diagram, thus the associated high frequencies.

simulator applicable to modeling CO_2 flow in deep saline aquifers. Two phases are considered: a CO_2-rich supercritical phase ("gas") and a H_2O-rich liquid phase. CO_2 density is computed using a cubic equation of state tuned to experimental measurements, while liquid density is corrected for total dissolved solids (TDS). Between the two phases, two components (CO_2, H_2O) are modeled; CO_2 and H_2O can exist in both phases. GASWAT first solves the pressure and molar density of each component. Mole fractions of the components in the phases are then computed through a flash process, where mutual solubilities of CO_2 and H_2O are calculated to match experimental data. Though another module (CO2STORE) has been cited, it is not used here due to the limitations in its applicable pressure (up to 8700 psi) and temperature (12~100°C) ranges. If 8700 psi is set as the injector BHP, CO_2 cannot be injected into the deeply buried reservoir at a sufficiently high rate. Maximum Nugget sandstone temperature near the injection site is ~110°C, which can be accommodated by GASWAT. With this option, temperature of the reservoir can vary with depth, which provides static values to determine fluid properties (no energy balance equation is solved). A temperature field is assigned to the model by interpolating and extrapolating data from temperature logs [*Li et al.*, 2011].

[23] Brine TDS is set at a uniform value of 77,487 ppm, reflecting a measured value near the injection site. To evaluate residual trapping, a hysteretic relative permeability function is assigned to the gas phase (Figure 3). A non-hysteretic function is assigned to the liquid phase, assuming that the rock matrix is water wet. Both functions are based on those measured in CO_2/brine experiments on the Viking Sandstone [*Bennion and Bachu*, 2005, 2006a, 2006b]. To model flow reversal in a grid cell before maximum gas saturation is reached, scanning curve interpolation between the bounding relative permeability curves is used [*Carlson*, 1981]. During simulations, a single pressure is calculated, assuming zero capillarity. Besides heterogeneity and mobility effects, CO_2 flow is typically dominated by viscous force during injection and gravity override after injection ceases.
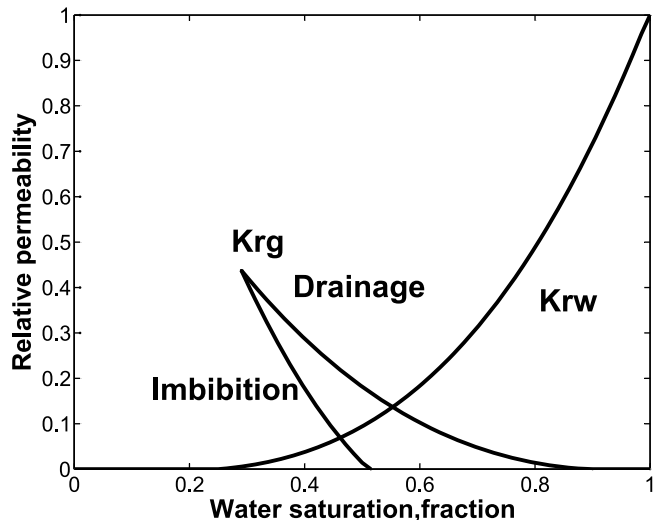
Figure 3. Relative permeability functions used in CO_2 simulations. Krg is relative permeability for the gas phase; Krw is relative permeability for the liquid phase.
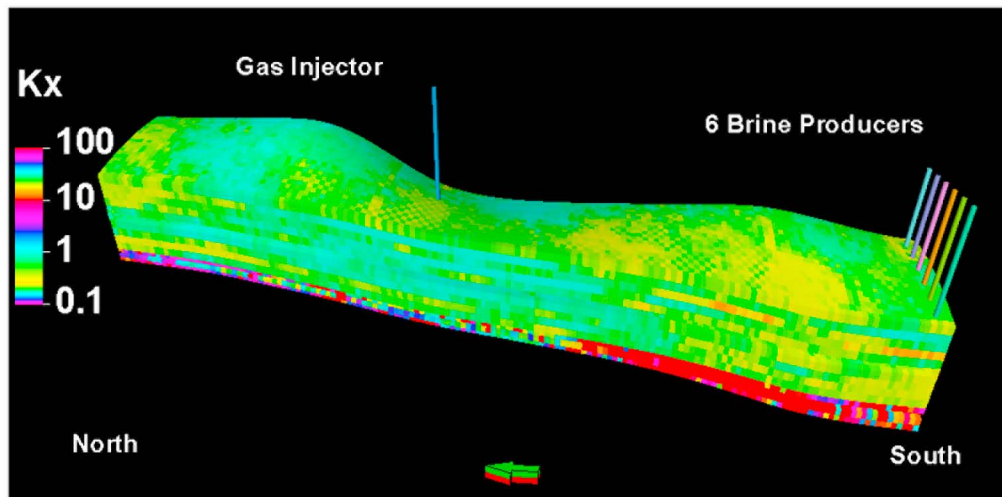
Figure 4. Location of the CO_2 injector and brine producers. Model shown is the FHRM. The injector is placed at Shute Creek gas plant, the proposed injection site.

Capillarity can locally enhance trapping, though it is not modeled here so as to simplify the upscaling analysis.

[24] To initialize the model and to compute fluid properties, an initial hydrostatic pressure distribution is assigned to the model which is fully saturated with the liquid phase. Rock compressibility is assigned using a typical value for sandstones (9.81×10^{-7} 1/psi assigned at a reference pressure of 5801 psi). A single injector is placed at the Shute Creek gas plant (proposed injection site), fully perforating the reservoir (Figure 4). An injection rate is set at 83,515 Mscf/d (1.70 Mt/year), for a duration of 600 years. The injection phase is followed by a 2500-year monitoring period, for a total simulation time of 3100 years. The injection time is chosen to be artificially large so as to maximize the filling of CO_2 in the reservoir when a single injector is used. The injection rate is also a target rate; the actual rate is modified by the simulator to satisfy a set of well constraints (discussed below). The actual rate can vary with time.

[25] To prevent geomechanical damage to the storage formation and overlying caprocks, an injector BHP constraint is set using $1.8 \times$ hydrostatic pressure at the reservoir depth (10,260 psi). This threshold is selected based on results of pressure leak-off tests (LOT) from two wells located near Shute Creek. LOT can be used to determine in situ fracture gradient of a formation. In the Nugget Sandstone, LOT yield an equivalent mud weight of about 1.8 g/cm^3, which translates to the above fracture gradient if fresh water density is used for formation fluid (1.0 g/cm^3). This fracture gradient is consistent with those estimated for many hydrocarbon fields [*Eaton*, 1969].

[26] During simulations, the injection rate is continuously adjusted by the simulator so that the maximum formation fluid pressure does not exceed the BHP constraint. However, the injector can eventually be shut down if no suitably small rate can be found to satisfy the constraint. To control pressure buildup, six brine producers are completed near the southern end of the model. The producers are downdip from the injector, each fully perforating the formation. (An opposite placement in the northern end will enhance updip migration and reduce the overall formation sweep; this option is not considered). When turned on (during the injection phase only), the producers are placed on a total fluid production rate constraint set equal to the CO_2 injection rate adjusted by reservoir volume. The producers act to create pressure drawdowns in the reservoir, simultaneously extracting brine and reducing pressure. This "voidage replacement" strategy is often used in reservoir modeling to simulate secondary recovery [*Kumar et al.*, 2005]. In this study, all rates were adjusted during an initial set of experiments, whereby the simulation progress was monitored for convergence issues. The final set of parameters give consistent and stable solutions for all models, e.g., during injection, both the CO_2 injector and brine producers (if turned on) are continuously operating without violating the BHP constraint.

[27] Boundary conditions (BC) of the model can profoundly influence the evolution of reservoir pressure, CO_2 plume, and formation sweep. Typical for deep aquifers (at the injection site, Nugget Sandstone lies at depth of ~13,000 ft), significant uncertainty exists in the nature of the reservoir compartment. Though well log correlation near the injection site suggests lateral continuity of the sandstone [*Li et al.*, 2011], extrapolation to regional scale is difficult due to lack of well control away from the site. Far west of Shute Creek, in an area called Wyoming-Utah Thrust Belt, the Nugget Sandstone is thrusted toward the surface. Here, the formation was observed to be compartmentalized by bounding faults [*Lindquist*, 1988]. In this study, end-member boundary conditions are tested to assess their impact on CO_2 storage. Four BC are investigated, with and without brine production. BC 1 is all-closed-no-brine, where all boundaries are no-flow (closed) and brine production is not activated. BC 2 is all-closed-with-brine, where all boundaries are closed, but brine production is turned on during CO_2 injection. BC 3 is open-no-brine, where all boundaries are closed except the north and south faces, where an open boundary is assigned. No brine is produced. BC 4 is open-with-brine, where north face is open and south face is closed, while brine production is activated during CO_2 injection. In all the simulations with brine production, the producers are shut down when CO_2 injection ceases, but the conditions at the boundaries

Table 2. Equivalent Permeability of the Upscaled Models Computed Using m = 3, 4, and 6[a]

Stratigraphic Model	Unit	m	Upscaled Permeability (mdarcy)					
			k_{xx}	k_{xy}	k_{xz}	k_{yy}	k_{yz}	k_{zz}
Facies	unit 1	3	22.61	0.22	−0.06	25.61	−0.11	1.36
		4	22.61	0.22	−0.05	25.62	−0.12	1.32
		6	22.60	0.22	−0.04	25.62	−0.13	1.29
	unit 2	3	17.31	0.12	0.06	19.41	0.13	0.98
		4	17.31	0.12	0.06	19.40	0.16	0.94
		6	17.31	0.12	0.07	19.40	0.15	0.90
	unit 3	3	7.14	1.55	0.38	23.08	−0.80	0.41
		4	7.34	1.83	0.20	22.24	−0.39	0.21
		6	7.40	1.91	0.14	21.99	−0.25	0.14
	unit 4	3	1014.70	137.12	−0.12	1082.16	−15.35	0.42
		4	1020.37	135.69	0.45	1077.41	−16.28	0.36
		6	1027.24	136.93	0.44	1065.18	−16.70	0.34
Layered	unit 1	3	20.99	0.21	0.15	23.89	−0.20	1.54
		4	20.99	0.21	0.15	23.89	−0.19	1.54
		6	20.99	0.21	0.15	23.89	−0.19	1.54
	unit 2	3	19.36	0.29	−0.07	21.52	0.12	0.98
		4	19.36	0.27	−0.05	21.58	0.14	0.91
		6	19.35	0.27	−0.04	21.58	0.13	0.86
	unit 3	3	302.86	72.42	−0.54	334.19	−4.92	0.36
		4	303.31	72.36	−0.67	332.66	−5.22	0.33
		6	304.09	72.34	−0.917	329.90	−5.703	0.32
Formation	unit 1	3	92.35	18.59	−0.02	96.89	−1.03	0.69
		4	92.36	18.58	−0.01	96.93	−1.02	0.64
		6	92.44	18.59	−0.08	96.69	−1.18	0.61

[a]See text for details. Location of the units is shown in Figure 1. When m = 4, the boundary conditions are x flow, y flow, z flow, and injection x flow. Two additional sets of experiments are conducted for m = 4, using x flow, y flow, z flow, and injection y flow and injection z flow, respectively. The upscaled permeability is very close to what is obtained with injection x flow. Results of these tests are not shown.

remain unchanged. The open boundary is modeled with the Fetkovich Aquifer Facility [*Schlumberger*, 2009], which allows the resident brine, and later the injected CO_2, to flow out of the model into an external aquifer where pressure response is assumed to be felt uniformly throughout. This in effect represents a reservoir that is semi-infinite in the direction where an open boundary is prescribed. The opposite situation of the closed system reflects the existence of sealing faults that act to compartmentalize the reservoir.

[28] To evaluate multiple conceptual models, all models are simulated under identical conditions (e.g., boundary condition, injection rate, brine production, well constraints), the only difference being that in the simple models, equivalent permeability and average bulk porosity are assigned to each model unit. Thus no calibration is attempted by varying the parameters of these models to fit the predictions of the FHRM. The bulk porosity is estimated by a volume-weighted average of the subunit cell porosities.

3. Results

3.1. Permeability Upscaling: Sensitivity Analysis

[29] To analyze the intrinsic permeability of the upscaled models, sensitivity analysis on the number of flow experiments (m) is conducted to understand whether the computed $\mathbf{k}^*$ is sensitive to m and the associated flow configuration. Up to six global boundary conditions are tested (m = 6): (1) x flow (specified heads along the west and east faces; no-flow on all other faces); (2) y flow (specified heads along the north and south faces; no-flow on all other faces); (3) z flow (specified heads along the top and bottom faces; no-flow on all other faces); (4) water is injected at a constant rate into the model center and all boundaries are closed except the east and west faces (i.e., injection-induced radial pattern dominated by flow

along the x axis or injection x flow); (5) water is injected at the same location and at the same rate and all boundaries are closed except the north and south faces (injection y flow); (6) water is injected at the same location and at the same rate and all boundaries are closed except the top and bottom faces (injection z flow). Note that experiments 1–3 create linear flood patterns. The specified heads are selected such that in each experiment, flow is driven toward the positive axis. Experiments 4–6 create diverging flow patterns where the water injector is fully perforating the reservoir. The upscaled permeability for each unit is calculated based on the first three experiments, then based on four experiments (x flow, y flow, z flow, and injection x flow or injection y flow or injection z flow; three sets of $\mathbf{k}^*$ are computed), and finally, based on all six experiments.

[30] Results suggest that for all units, $\mathbf{k}^*$ are diagonally dominant full tensors (Table 2). All $\mathbf{k}^*$ have also passed the positive-definiteness test; no physically incorrect values were found. The diagonal dominance reflects the nearly flat stratification in the FHRM and the fact that heterogeneity principal correlation axes are approximately parallel to the simulation axes (Figure 1). Because of stratification, the lateral components of $\mathbf{k}^*$ (e.g., k_{xx}, k_{yy}) are also greater than the vertical components (e.g., k_{zz}), as expected. Unit 4 of the facies model has much higher equivalent permeability than unit 3 of the same model (both lie in the lower reservoir), attesting to the fact that the facies model has captured the bimodal distribution in this region by separating the deposit into two units. In the layered model, the lower reservoir is represented by its own unit 3, whose $\mathbf{k}^*$ lies between those of units 3 and 4 of the facies model. Further, $\mathbf{k}^*$ of units 1 and 2 of the facies model are similar to those of units 1 and 2 of the layered model, despite the different division scheme. These four units lie in the thicker upper reservoir, where the level of

Table 3. Aquifer Inflow Rates Computed By All Models[a]

Permeability Model	X Flow (W-E)		Y Flow (N-S)		Z Flow (Vertical)	
	QR	Error(%)	QR	Error(%)	QR	Error(%)
FHRM	56161.25	-	44248.63	-	19413.37	-
Facies	49368.26	−12.87	36021.43	−20.50	19408.29	−0.03
Layered	57219.8	1.87	47622.66	7.35	19254.10	−0.82
Formation	63305.82	11.96	57323.73	25.75	19322.87	−0.47

[a]QR is aquifer inflow rate. For each upscaled model, a percent error is computed based on the results of the FHRM.

variability is low. The lateral components of k^* of these units range from 17.3 to 25.6 mdarcy, encompassing the median value of the full distribution (21.0 mdarcy). In the formation model, only a single k^* is computed.

[31] Table 2 also lists the components of k^* computed using each of the flow configurations. By comparing their values, changes in k^* are observed to be small. For example, for the layered model the largest change in k^* components is 0.4% (between $m = 3$ and 4) and 1.3% (between $m = 3$ and 6); for the facies model the largest change is 0.6% and 1.6%, respectively; for the formation model, the largest change is 6.7% and 0.2%, respectively. This suggests that k^* is mostly insensitive to the number of flow experiments used in upscaling and the associated flow patterns. The additional nonlinear flow experiments do not significantly influence the upscaled permeability compared to those obtained with linear floods. The upscaled permeability obtained from linear flow experiments (i.e., $m = 3$) are used in subsequent single-phase verification tests and CO_2 storage modeling.

3.2. Permeability Upscaling: Verification Tests

[32] Equivalent permeability computed for the upscaled models is verified by conducting single-phase (water), steady-state, incompressible flow simulations in all models, with the FHRM providing reference predictions. The same boundary conditions used in upscaling (i.e., x flow, y flow, z flow) are tested, following *Zhang et al.* [2006]. Three sets of Constant-Head Darcy tests are conducted, with each set simulating all models driven by the same boundary condition. Each upscaled model computes an aquifer inflow rate, i.e., flow rate between an external aquifer of higher head and the reservoir model (Table 3). A percent relative error is computed based on the flow rate of the FHRM. This error ranges from less than 1% to 26%, with the z flow simulations generally the most accurate. (An outflow rate, between the reservoir model and an external aquifer of lower head, is also computed. At steady-state, its value is verified to be nearly identical to the inflow rate and is thus not shown.)

[33] To assess the accuracy in predicting fluid potential, a mean error (ME) is defined for each upscaled model:

$$\text{ME} = \frac{1}{n} \sum_{i=1}^{n} \left| \Phi_{fw}^{(i)} - \Phi_{ref}^{(i)} \right| \qquad (2)$$

where $\Phi_{fw}^{(i)}$ represents fluid potential of the ith grid cell computed by an upscaled model, $\Phi_{ref}^{(i)}$ represents the same fluid potential of the FHRM, and n is the total number of grid cells in the model. A dimensionless mean relative error (MRE) is also computed by normalizing ME with absolute potential drop across the model which drives flow (Table 4). The MRE ranges from less than 1% to 11%, with the facies model consistently being the most accurate.

[34] Histogram of the prediction error in fluid potential ($\Delta\Phi = \Phi_{fw} - \Phi_{ref}$) is also shown for each model, one for each boundary condition tested. Under the same boundary condition, the potential drop used to drive flow through the models is the same. But, for the same model (Figure 5), the potential drop varies with boundary condition. The histogram ranges from unimodal to bimodal, with a similar distribution when models are simulated under the same boundary condition. Flow direction thus controls the shapes of the error histograms rather than difference in conceptual models. Under the same boundary condition, $\Delta\Phi$ range is consistently the smallest for the facies model. For the layered and formation models, the spread of $\Delta\Phi$ is larger, although they are similar in magnitude.

[35] The above results suggest that accuracy in flow rate prediction appears to be controlled by boundary condition (i.e., whether flow is parallel or perpendicular to stratification), while accuracy in fluid potential prediction appears to be controlled by the model (i.e., finer heterogeneity resolution has better accuracy). The magnitude of flow rate prediction error does not correspond to the magnitude of fluid potential prediction error, e.g., the facies model is not necessarily the most accurate in flow rate prediction. This suggests that when multiple boundary conditions are considered, no model is best in predicting both flow rate and fluid potential. The magnitude of the errors, however, is considered acceptable compared to those encountered in previous studies. For example, 2-D results of *Zhang et al.* [2006] gave rise to a maximum flow rate prediction error of −31% and a maximum head prediction MRE of 9%. In that study, errors were also found to be sensitive to boundary condition and homogenization level. Given the overall compatibility of the results with the expected error margins, the upscaled models are considered adequate to represent the FHRM as equivalent models for single-phase processes.

3.3. CO_2 Flow Modeling

[36] Commercial-scale CO_2 injection is simulated in all models until the reservoir is sufficiently filled, followed by postinjection simulation to monitor plume migration. To understand pressure buildup in the reservoir, two boundary conditions are tested to represent a reservoir that is compartmentalized and one that is open on the sides (in this case, brine will be displaced out of the reservoir into an external aquifer). These two conditions define end-member scenarios, given the uncertainty of the boundary condition at the injection site. To also address injectivity, for half of the runs, six brine producers will operate during CO_2 injection. Finally, to evaluate performance of the upscaled models against that of the FHRM, four prediction metrics are used.

[37] 1. The first is total predicted gas-in-place (GIP) and gas storage ratio (GSR) at the end of the simulation (Table 5). GSR is mass fraction of the total dissolved and trapped gas in GIP. It is less than 1.0 due to the existence of mobile gas.

Table 4. MRE in Fluid Potential Computed for Each Upscaled Model

Permeability Model	X Flow (W-E) MRE (%)	Y Flow (N-S) MRE (%)	Z Flow (Vertical) MRE (%)
Facies	2.24	4.28	0.37
Layered	4.18	10.57	0.64
Formation	4.16	9.84	0.94
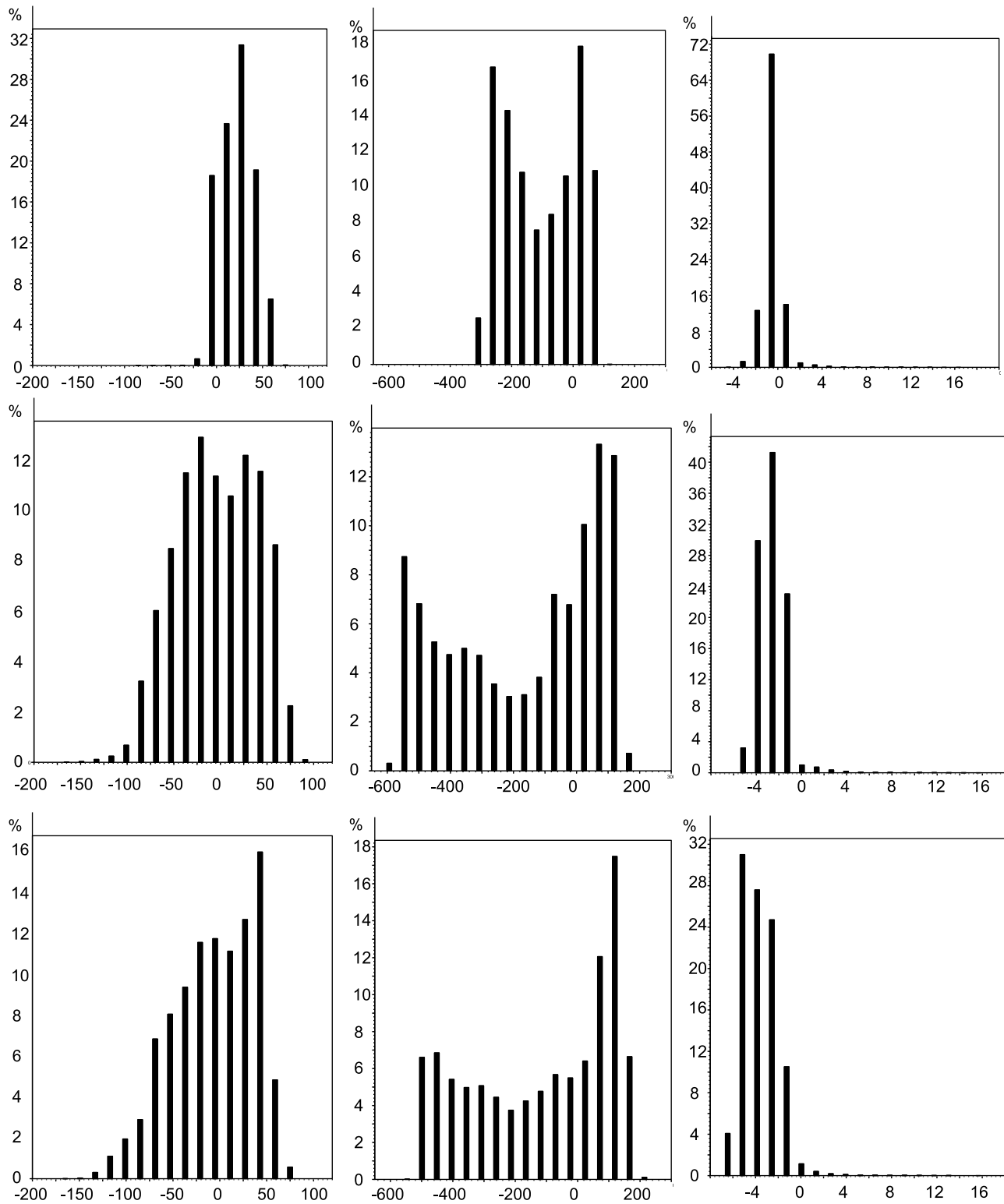
Figure 5. Histogram of the prediction error in fluid potential ($\Delta\Phi = \Phi_{fw} - \Phi_{ref}$; in psi) for each upscaled model, under (left) x flow, (middle) y flow, and (right) z flow conditions. (top) Facies model; (middle) layered model; (bottom) formation model.

[38] 2. The second is average reservoir fluid pressure and its evolution over time. It is lower than the injector BHP but greater than the producer BHP (if activated).

[39] 3. The third is gas saturation map and its evolution over time.

[40] 4. The fourth is total predicted gas (in mass unit) over time or gas profiles.

[41] In Table 5, results pertaining to the first performance metric are presented for all boundary conditions. In all gas categories, facies and formation models are more accurate

Table 5. Gas-in-Place in the Reservoir Predicted By All Models at the End of Simulation[a]

| Model | BC | Gas-in-Place (lb mol) ($\times 10^{10}$) | | | | Storage Ratio (%) | Total Injected Gas | | Injection Time (years) | Injection Rate (Mt/yr) |
		Dissolved	Trapped	Mobile	Total		Pound Mole ($\times 10^{10}$)	Megaton		
FHRM	1	0.03	0.16	0.04	0.23	0.84	0.23	44.47	50	0.89
	2	0.20	1.97	1.72	3.89	0.56	4.23	817.87	600	1.36
	3	0.32	2.92	2.21	5.45	0.59	5.49	1061.49	600	1.77
	4	0.24	2.14	1.62	4.00	0.60	5.10	986.09	600	1.64
Facies	1	0.03	0.17	0.03	0.23	0.87	0.23	44.47	50	0.89
	2	0.20	2.09	1.70	3.99	0.57	4.12	796.60	600	1.33
	3	0.32	2.81	2.31	5.44	0.58	5.48	1059.56	600	1.77
	4	0.25	2.28	1.59	4.12	0.61	5.03	972.55	600	1.62
Layered	1	0.03	0.17	0.03	0.23	0.87	0.23	44.47	50	0.89
	2	0.21	1.78	1.26	3.25	0.61	3.52	680.59	600	1.13
	3	0.21	2.10	1.97	4.28	0.54	4.36	843.01	600	1.41
	4	0.23	2.00	1.36	3.59	0.62	5.04	974.48	600	1.62
Formation	1	0.03	0.17	0.03	0.23	0.86	0.23	44.47	40	1.11
	2	0.21	2.22	1.76	4.19	0.58	4.35	841.07	600	1.41
	3	0.18	2.29	2.88	5.35	0.46	5.37	1038.29	600	1.73
	4	0.23	2.49	2.38	5.10	0.53	5.13	991.89	600	1.65

[a]GIP is gas-in-place. Four boundary conditions are tested (see text for details). The total injected gas is listed, as well as the actual injection rate. For some cases, CO_2 has flowed out of the reservoir; thus total GIP < total injected gas. A CO_2 storage ratio is defined as (Dissolved GIP + Trapped GIP)/Total GIP × 100%. For BC 1, the injection time is defined by the time when the actual injection rate is larger than 1000 Mscf/day.

than the layered model. For all models, BC 1 results in much less CO_2 being injected, but the highest GSR. In a sealed system, the injector is shut down when the BHP constraint is reached. The higher ratio may have been due to the fact that formation fluid pressure in BC 1 simulations is the highest among all boundary conditions tested. Higher pressure leads to more CO_2 dissolution in brine as well as to higher gas saturation at the end of injection. This higher gas saturation, in turn, leads to more residual trapping, following a scanning curve that is closer to the bounding imbibition curve. Simulations under BC 2, 3, and 4, however, lead to similar GSR, but the amount of total gas injected and total gas stored vary by ~27%. This suggests that, given the current well constraint, boundary conditions can impact the amount of gas that can be injected and subsequently stored in the reservoir.

[42] For each simulation case, the actual injection rate achieved is computed by dividing the total injected gas by the duration of injection (Table 5). It ranges from 0.89~1.77 Mt/year, with BC 3 and 4 predicting higher rates. Considering that these cases simulate a reservoir linked to an infinitely large external aquifer, this result is expected. With one injector, the actual operation rate will likely lie within the above range, between a completely sealed and a completely open system. However, the simulations use an artificially long injection time to create a single plume to fill the reservoir. In actuality, the injection time will be shorter, corresponding to the lifetime of power plants. If a single injector is used, the extent of the actual plume at the decommission time will be much smaller than those simulated here. Clearly, realistic simulations will require more injectors operating over shorter times. Such scenarios will be presented in section 4. The focus of this section is conceptual and does not reflect actual practices.

[43] Under boundary conditions 2, 3, and 4, which are of greater interest, the dominant flow of CO_2 in the formation is lateral and upward during injection, driven by the pressure gradient in the reservoir and buoyancy of the CO_2. After injection ceases, gravity override dominates. The gas-phase plume continues to rise, spreading out beneath the formation top. At the end of simulation, a laterally extensive high-saturation zone, consisting mostly of mobile CO_2, can be

observed. This postinjection gravity segregation is significant, owing to the fairly high vertical permeability of the models (i.e., cell permeability of the FHRM is weakly anisotropic while permeability of the upscaled models is derived from those of the FHRM). Beneath this mobile high-saturation zone, reservoir cells are dominated by trapped CO_2, often at or below the residual gas saturation (0.48). This fraction of the gas plume is immobile and will not migrate further.

[44] In sections 3.3.1–3.3.5, for each boundary condition tested, time profiles of average reservoir pressure, saturation, and gas predictions are presented. Gas saturation is visualized along a north-south transect through the model, crossing the injector at Shute Creek. The saturation shown is the total combined mobile and trapped CO_2. Dissolved CO_2 in formation brine is not shown. The dissolved plume has a shape similar to the gas-phase plume, but its (aqueous) concentration is more uniformly distributed in space.

3.3.1. BC 1: All-Closed-No-Brine

[45] Under this BC, fluid pressure rises quickly in all models from the initial hydrostatic pressure (~5700 psi), and the injector is shut down when the reservoir pressure reaches the BHP constraint after ~50 years of simulation (Figure 6). The gas-phase plume is small at the end of 600 years (reservoir is still monitored after the injector is shut down), filling a small part of the formation near the injector. During the actual injection time, the average rate is ~0.89 Mt/year, too small to sustain a commercial operation. All models predict similar pressure as well as shape and size of the gas- and dissolved-phase plumes (not shown). Under this extreme condition of low injectivity, gas migration is limited and all models are approximately of equal accuracy.

3.3.2. BC 2: All-Closed-With-Brine

[46] With brine production, significantly more CO_2 can be injected into the reservoir and formation pressure never exceeds the BHP constraint (Figure 7). During injection, the average reservoir pressure drops gradually until reaching a steady, subhydrostatic value (~3800 psi) at the end of injection (600 years; 219,000 days). This is due to brine production. The level of pressure drop is controlled by the water rate, e.g., larger drop can result from higher production rate (when
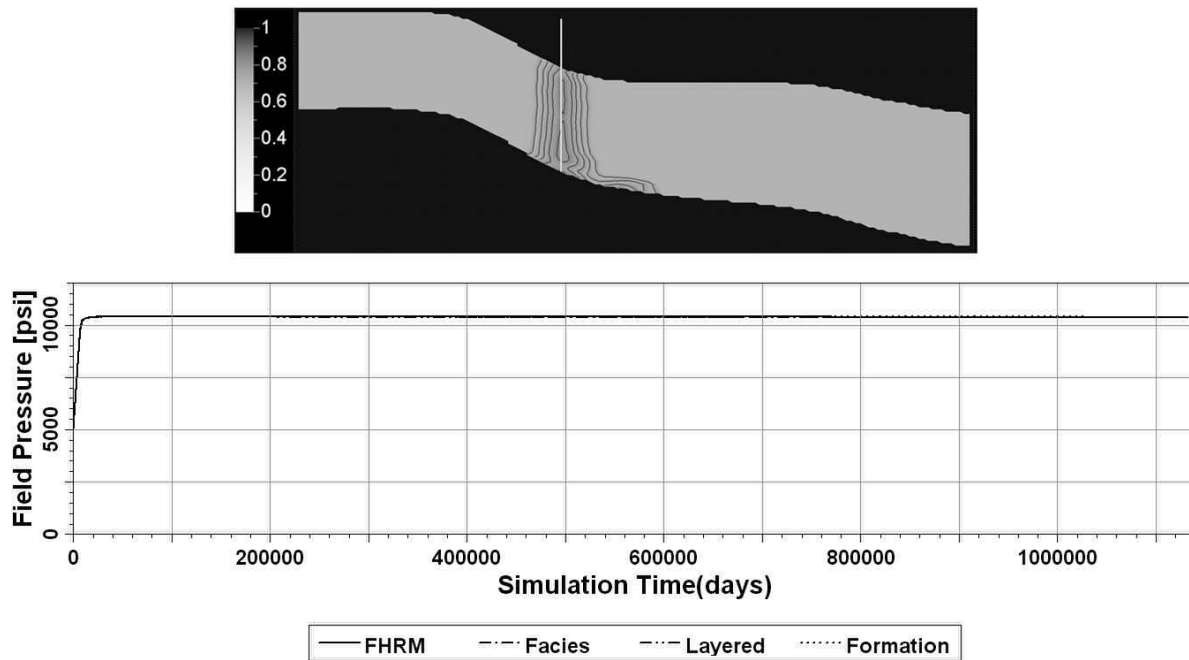
Figure 6. BC 1, all-closed-no-brine. (top) Gas-phase CO_2 saturation along a north-south transect after 600 years of simulations. Shown is the prediction by the FHRM. (bottom) Average reservoir pressure over time predicted by all models.

the voidage constraint is removed). All models simulate a large regional-scale plume, with the facies model being the most accurate in reproducing the plume shape of the FHRM, at both time scales (i.e., end-of-injection and end-of-monitoring). It is also the most accurate in predicting the pressure profile. The layered model appears to be the least accurate in predicting both pressure and plume shape, e.g., a tongue of gas plume is seen in the lower reservoir which is absent in the FHRM. The predictions of the formation model are not significantly different from those of the facies model. Despite a slightly larger deviation in predicting the pressure profile, it is sufficiently accurate to predict the extent of the plume footprint at both time scales. Overall, predictions of the upscaled models are not significantly different from those of the FHRM.

3.3.3. BC 3: Open-No-Brine

[47] Under this BC, again, significant amounts of CO_2 can be injected into the reservoir and formation pressure never exceeds the BHP constraint (Figure 8). However, compared to the pressure profiles of BC 2, pressure rises in all models during injection and then drops to the preinjection level later on. This rise (with the exception of the layered model) is gradual and pressure buildup in the reservoir is small. This is because, during injection, formation brine is continuously being displaced into the external aquifer through the open boundaries. Pressure buildup near the injector is thus continuously attenuated.

[48] With the exception of the layered model, all models predict a large, regional-scale plume, with significant updip (mobile) gas migration occurring during monitoring. Accordingly, in these three models (FHRM, facies, formation), sweep efficiency is higher in the updip region. This updip migration is more significant compared to that predicted by the same models under BC 2, where brine producers create pressure drawdown in the south which counteracts updip flow. Among all the upscaled models, the facies model is again the most accurate in both plume shape and pressure predictions, and the layered model is the least accurate. The formation model predicts the high-saturation mobile gas zone reasonably well, though it underestimates the extent of the trapped gas in the downdip reservoir. In this model, despite its reasonable pressure prediction, lack of heterogeneity results in less plume spreading and, as a result, less trapping. In BC 2, however, formation model is comparatively more accurate; brine production in that case enhances downdip sweep and thus trapping, despite the lack of heterogeneity.

[49] Gas plume predicted by the layered model is significantly different from those of the other models, with most of the injected CO_2 channeling through the lower unit to reach and escape through the open boundaries on the north and south sides. This feature persists during repeated simulations when results are inspected at earlier times; it is an authentic outcome, which develops soon after the injection starts. The lower unit of this model, which contains a bimodal permeability distribution (Figure 2), is homogenized by a single equivalent **k***. Though single-phase tests under linear floods do not indicate significant errors in flow rate and fluid potential predictions (they are similar in magnitude to those estimated for the facies and formation models), such an equivalent **k***appears inadequate in two-phase modeling. Compared to the facies model that conforms to heterogeneity, the layered model averages permeabilities from grid cells belonging to facies with different mean k. Though this does not cause problems in single-phase prediction, it is sufficiently inaccurate for CO_2 modeling, which is additionally affected by mobility, gravity, and flow rate (i.e., strength of the viscous driving force). The pressure profile predicted by this model is also the least accurate. It rises higher during
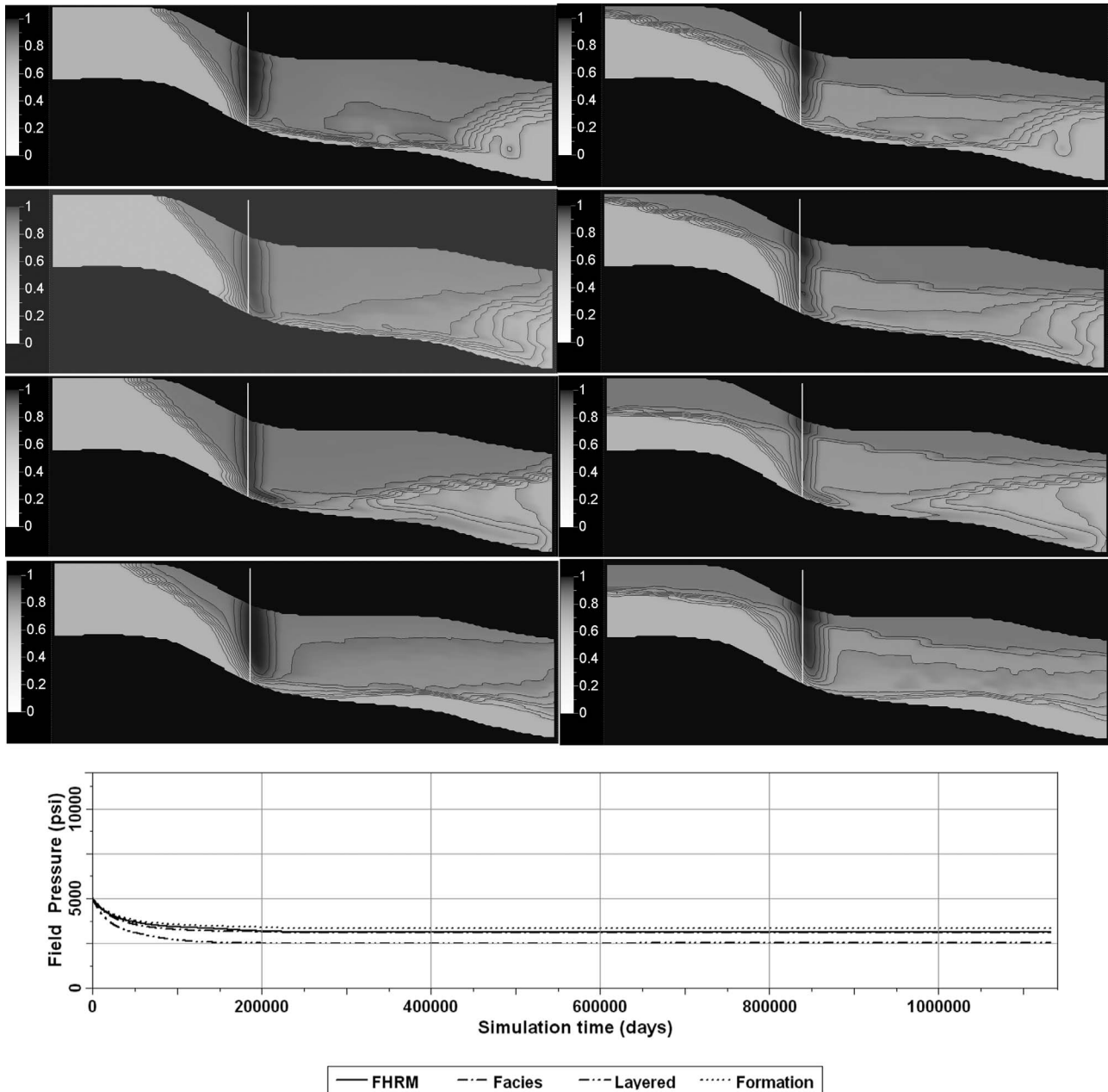
Figure 7. BC 2, all-closed-with-brine. (top) Gas-phase CO_2 saturation along the same transect of Figure 6. (left) End of injection (600 years or 219,000 days) and (right) end of monitoring. First row is FHRM; second row is facies model; third row is layered model; fourth row is formation model. (bottom) Average reservoir pressure over time predicted by all models.
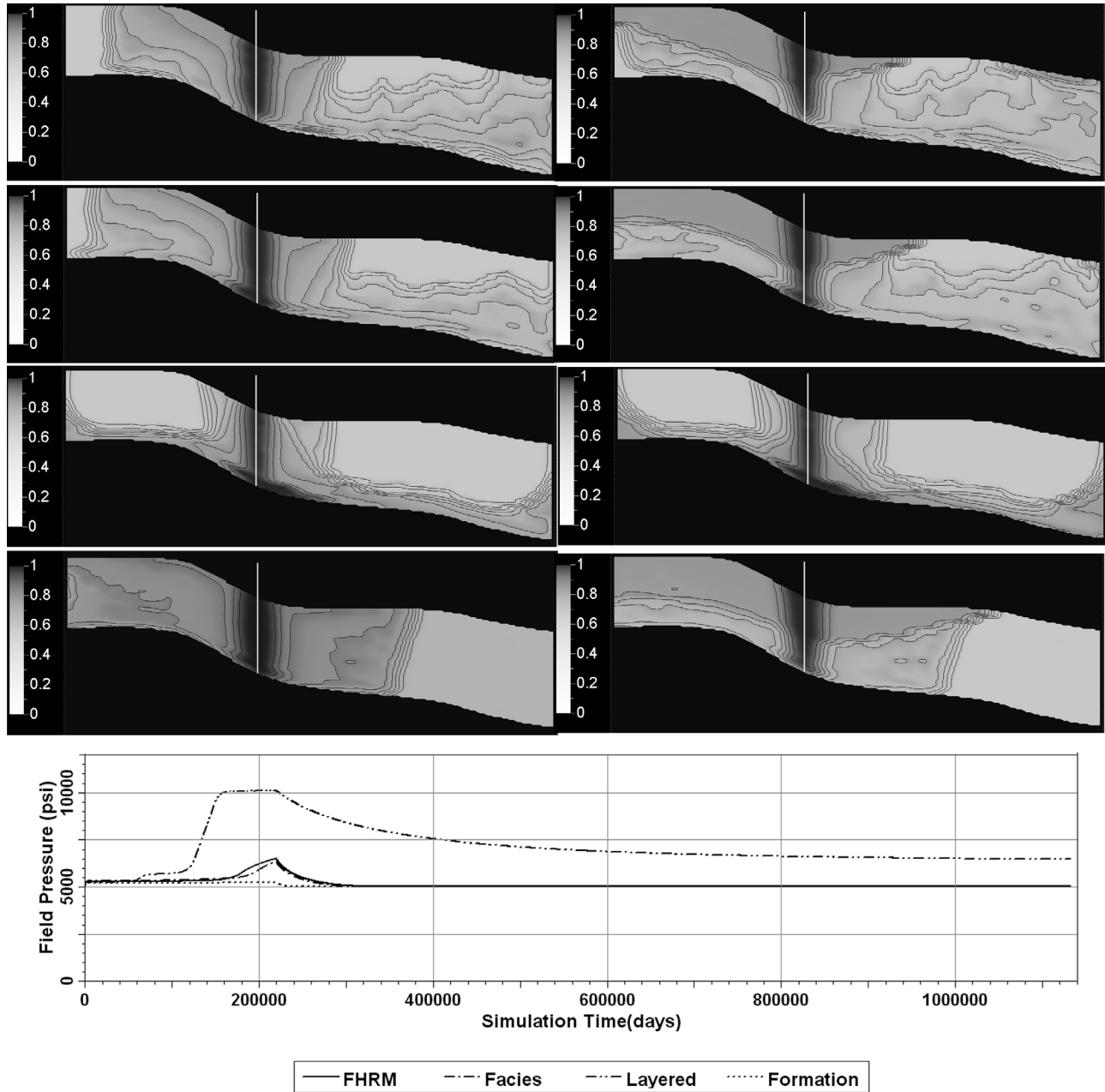
Figure 8. BC 3, open-no-brine. (top) Gas-phase CO_2 saturation. (left) End of injection and (right) end of monitoring. First row is FHRM; second row is facies model; third row is layered model; fourth row is formation model. (bottom) Average reservoir pressure over time predicted by all models.
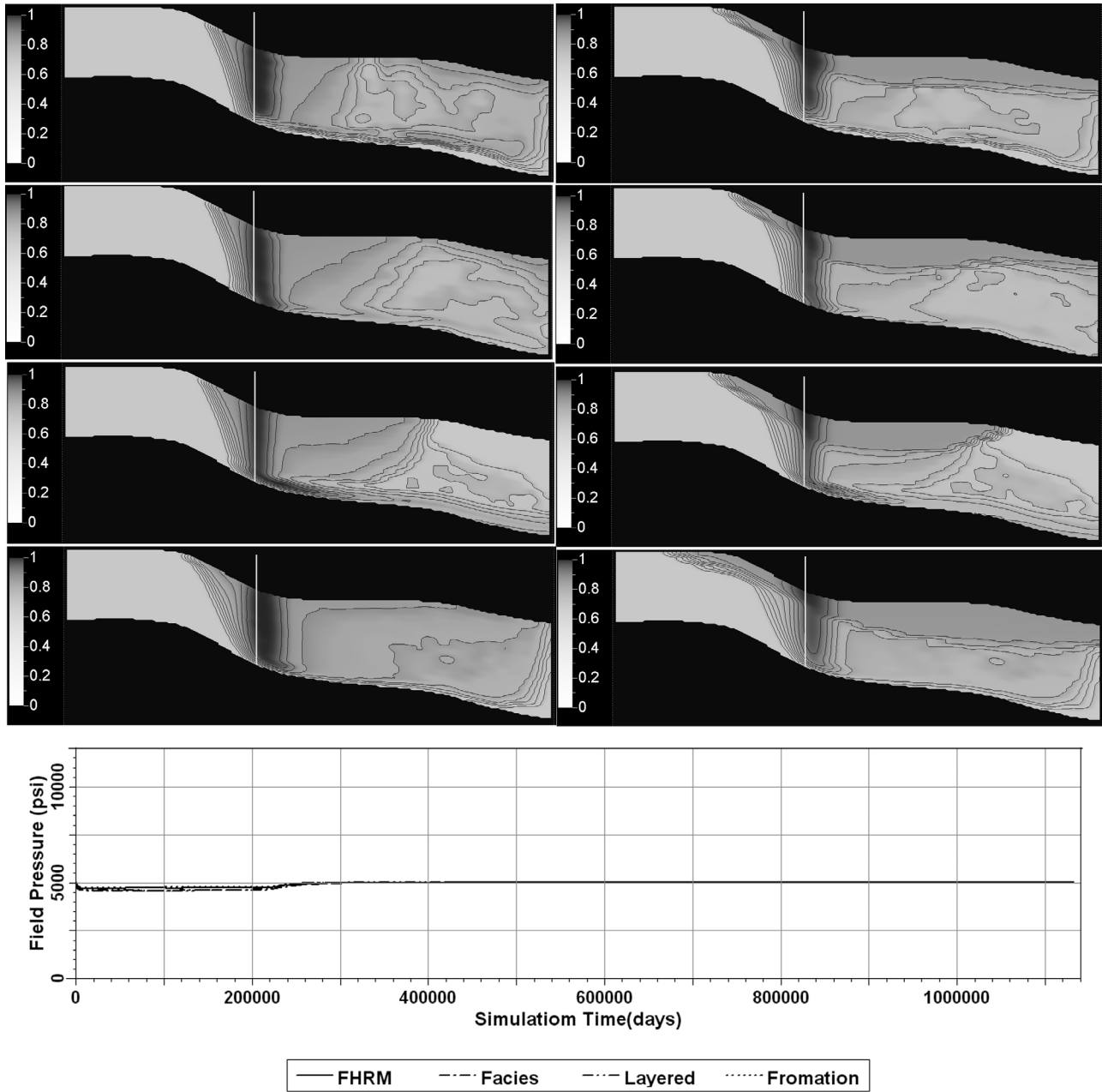
Figure 9. BC 4, open–with–brine. (top) Gas-phase CO_2 saturation. (left) End of injection and (right) end of monitoring. First row is FHRM; second row is facies model; third row is layered model; fourth row is formation model. (bottom) Average reservoir pressure over time predicted by all models.
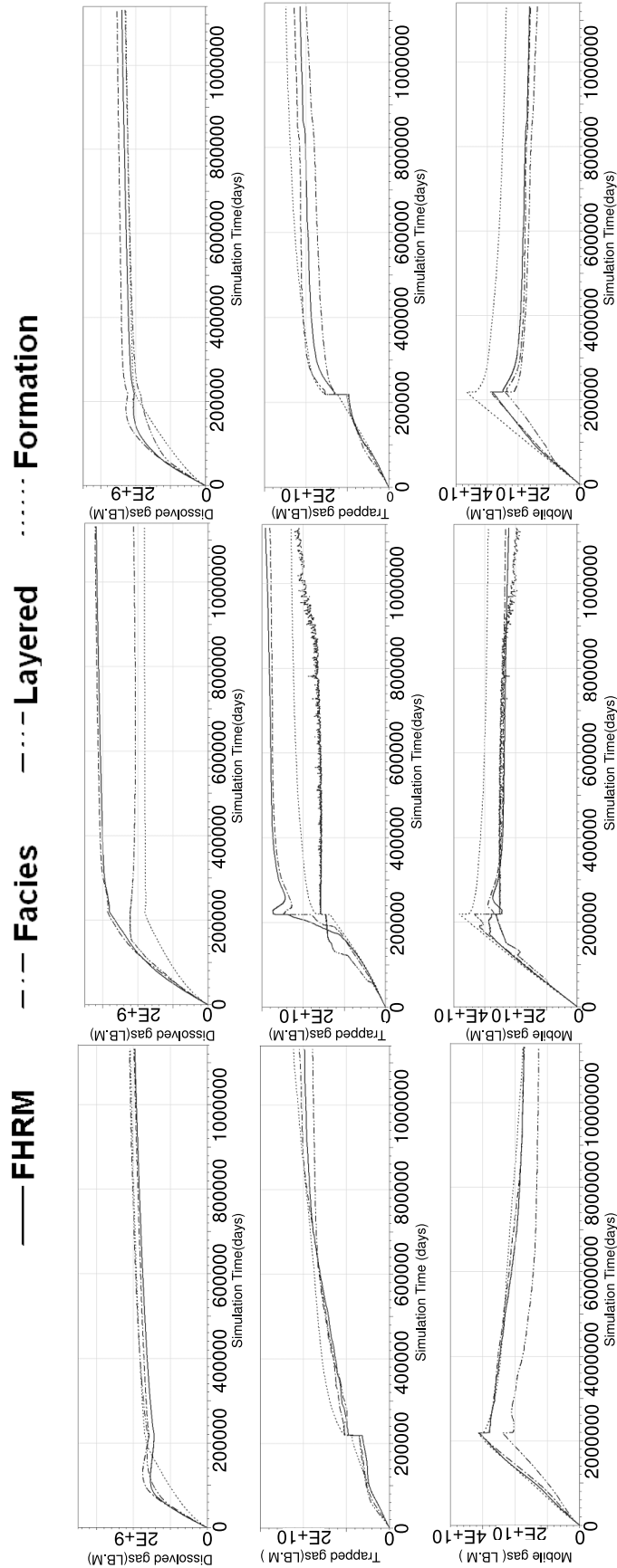
Figure 10. Gas-in-place over time predicted by all models under BC 2, 3, and 4. (left) BC 2; (middle) BC 3; (right) BC 4.

injection compared to those predicted by the other models. At ~160,000 days (438 years), it reaches the BHP constraint and the injection rate is adjusted downward to maintain a lower pressure until the end of injection (the simulator is able to find lower enough rates so that the injector is not shut down). This is not the behavior of the FHRM.

3.3.4. BC 4: Open-With-Brine

[50] Under this BC, the main difference from BC 3 is that brine producers are active during CO_2 injection. Several important differences are noted from the results of BC 3. First, average pressure profiles predicted by all models are nearly equally accurate. Owing to the producer rate constraint, all pressures are maintained at approximately the initial value. Clearly, brine production exerts an important control on the evolution of formation pressure. Second, during the injection phase, in all models, the dominantly updip migration (Figure 8) is replaced by downdip migration (Figure 9). Accordingly, all models predict more sweep efficiency and trapping in the downdip region. Clearly, brine production exerts an important control on the direction of the mobile gas flow. Third, the facies model, though again the most accurate, is not significantly more accurate than the other upscaled models. The layered model, though again the least accurate, is not as incorrect as it is simulated in BC 3. This is similar to what is observed in simulations under BC 2. These results suggest that brine production overrides the effect of heterogeneity, making the reservoir appear more homogeneous. In other words, the importance of representing heterogeneity with higher geologic resolution and realism (i.e., facies model), which is shown to be important in BC 3 simulations, is significantly dampened. In BC 3, without brine production, how heterogeneity is represented is clearly important in determining the relative accuracy of the upscaled models.

3.3.5. CO_2 Mass Profiles

[51] For the last performance metric, dissolved, mobile, and trapped CO_2 computed by all models are shown over time, under BC 2, 3, and 4 (Figure 10). In all models, with increasing time, more gas dissolves into brine, as expected. During injection, more gas is dissolved per unit time than during monitoring (observed change in slope at the end of injection), likely due to the fact that per unit time, more grid cells are swept during injection. More cells are contacted by gas, thus more dissolution. Once injection ceases, fluid velocity becomes smaller (dominated by the slow and upward gravity segregation), and fewer cells are contacted by gas per unit time. Though gas dissolution is also affected by reservoir pressure, the level of pressure variation does not significantly impact the rate of gas dissolution, e.g., during injection, average pressure is dropping in BC 2, rising in BC 3, and maintaining a stable value in BC 4. Flow effect appears to dominate gas dissolution rate, compared to the effect of pressure variation.

[52] The trapped gas also grows over time, as CO_2 migrates continuously in lateral and vertical directions, resulting in residual trapping. Additional trapping also occurs due to the nonnegligible critical gas saturation assigned to the CO_2 relative permeability drainage curve. Growth rate of the trapped gas is higher during injection. At this stage, higher fluid velocity in the reservoir again results in more cells being swept by gas per unit time. After the injection ceases, most trapping likely occurs at the trailing edge of the plume during the slow upward migration.

[53] The mobile gas grows linearly during injection, since the total amount of the injected gas is increasing. After the injection ceases, the amount of the mobile gas drops gradually, corresponding to the simultaneous increase of both the trapped and dissolved gas.

[54] Similar to what is observed with the plume shape, for all the gas categories, throughout the simulation time, when BC 2 and 4 are used (brine producers are active), variability of the predictions by the upscaled models is smaller and the predictions themselves are more accurate. Without brine production, as in BC 3, the facies model is again significantly more accurate than the layered and formation models.

4. Discussions

[55] Feasibility studies on CO_2 storage in deep saline aquifers use reservoir simulation with a geologic site model. However, multiple conceptual models can be developed depending on data support. Since increased costs can be incurred from building more complex models, it is important to identify an optimal heterogeneity resolution in such models which can provide adequate predictions in CO_2 modeling. However, in simulating CO_2 flow, gas migration and trapping are affected by multiple processes, e.g., viscous flow from active engineering (i.e., injection and production), mobility effect (i.e., different relative permeabilities and fluid viscosities), gravity segregation, formation heterogeneity, chemical reactions (only dissolution is modeled here), and site boundary condition. Since these processes operate and interact over varying spatial and temporal scales, the assessment of model complexity (i.e., identification of an appropriately simple site model) is not straightforward. In this study, multiscale permeability upscaling is combined with a sensitivity study on model boundary condition to identify an optimal model complexity in developing a reservoir model for CO_2 simulation. Several insights are gained and are discussed as follows:

[56] In permeability upscaling, equivalent permeability (one obtained for each unit of the upscaled models) is found to be largely insensitive to the number of flow experiments used and the associated flow patterns. Simple linear floods appear to provide sufficient information for its calculation without the need to introduce complex flow patterns. This is consistent with the results of *Zhang et al.* [2006]. This could be due to the fact that when the upscaling domain is large compared to the characteristic size of heterogeneity (i.e., ln$k$ correlation ranges), equivalent permeability can approach an effective value that is independent of the boundary condition used in upscaling [*Renard and de Marsily*, 1997]. Thus the upscaling domain in this study is suitably large for the calculation of a stable $\mathbf{k}^*$. In Nugget sandstone variogram modeling of facies-specific ϕ generally yields ϕ correlation ranges that are smaller than the size of the encompassing facies unit [*Li et al.*, 2011]. Correlation ranges of ln$k$ are also smaller, due to the linear $\phi - \log(k)$ transforms used to populate k from ϕ (one for each facies). For the layered and formation models, the size of their units is even larger. In addition, unlike past research where model domains for upscaling were contiguous [*Zhang et al.*, 2006], in this study, the shape of the facies units is extremely discontinuous, reflecting the geostatistical algorithms used in facies modeling (Sequential Indicator Simulation). Still, $\mathbf{k}^*$ of the facies units are stable and physically reasonable, i.e., error characteristics in single-phase verification tests are consistent with those observed in past work.
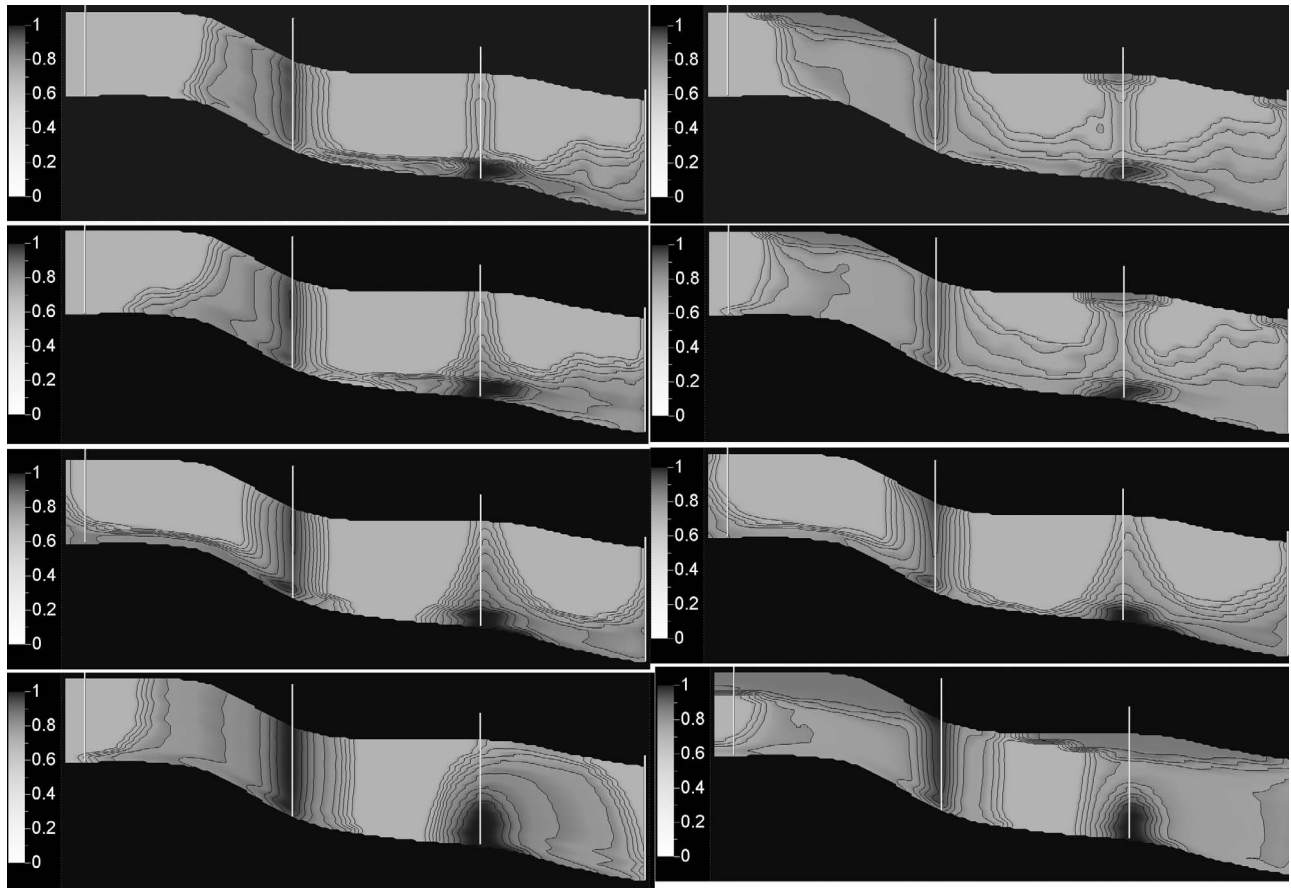
Figure 11. BC 3, open-no-brine, with two injectors (producers are inactivated). Gas-phase CO_2 saturation. (left) End of injection (50 years) and (right) end of monitoring. First row is FHRM; second row is facies model; third row is layered model; fourth row is formation model.

[57] In CO_2 modeling, for the spatial and temporal scales considered, without brine production, optimal complexity of the upscaled model is found to depend on the prediction metric of interest. The facies model is the most accurate at capturing plume shape, fluid pressure, and CO_2 mass profiles, while the formation model is adequate for pressure prediction. The layered model is not accurate for predicting most of the performance metrics, suggesting that both heterogeneity resolution and homogenization strategy are important to obtaining accurate predictions by the simple models. In terms of resolution, facies rather than the formation model is required if detailed plume shape is of interest. However, the layered configuration, despite its higher resolution than the formation model, is less accurate. Heterogeneity in the facies model is characterized by an underlying unimodal lognormal k. In the layered and formations models, for some units, heterogeneity is homogenized over multimodal distributions. This suggests that k* obtained for model units with unimodal distributions is more accurate for multiphase prediction.

[58] Boundary condition is found to impact not only formation fluid pressure but also how much CO_2 can be injected. If the reservoir is compartmentalized, brine production can control and modulate pressure buildup as well as enhance CO_2 injectivity. If the reservoir is not compartmentalized, brine production does not significantly impact pressure but can affect the direction of mobile gas flow. Importantly, the adequacy of an upscaled model in predicting CO_2 storage is affected by brine production; the importance of detailed heterogeneity resolution is weakened when the viscous force is strengthened in relation to the gravity force, i.e., increased lateral pressure gradient established by brine production in addition to that created by CO_2 injection. Thus when flow is more viscous dominated, variability of the predictions by the upscaled models becomes smaller and the predictions are more accurate, suggesting a subtle but important interplay between heterogeneity resolution, fluid driving forces, and model predictions. Brine production, besides being useful for controlling fluid pressure, has the potential benefit of offsetting conceptual model uncertainty. This observation has implications for modeling CO_2 storage in data-poor settings, where an efficient and cost-effective strategy is needed to build a site model. For example, if brine production is employed, a simple model will perhaps suffice for the predictions of both plume shape and reservoir pressure.

[59] The above observations, however, cannot be generalized easily, since they are based on one FHRM with a fixed heterogeneity pattern and variance. With a single injector, very long injection time was used, but realistic cases will likely use multiple injectors operating over shorter times. To test the results under more realistic conditions, additional simulations are conducted with BC 3 (no brine production) and BC 4 (brine production). Using the same constraints (e.g., injector BHP, voidage replacement if applicable), following a streamline analysis in the FHRM to identify main reservoir
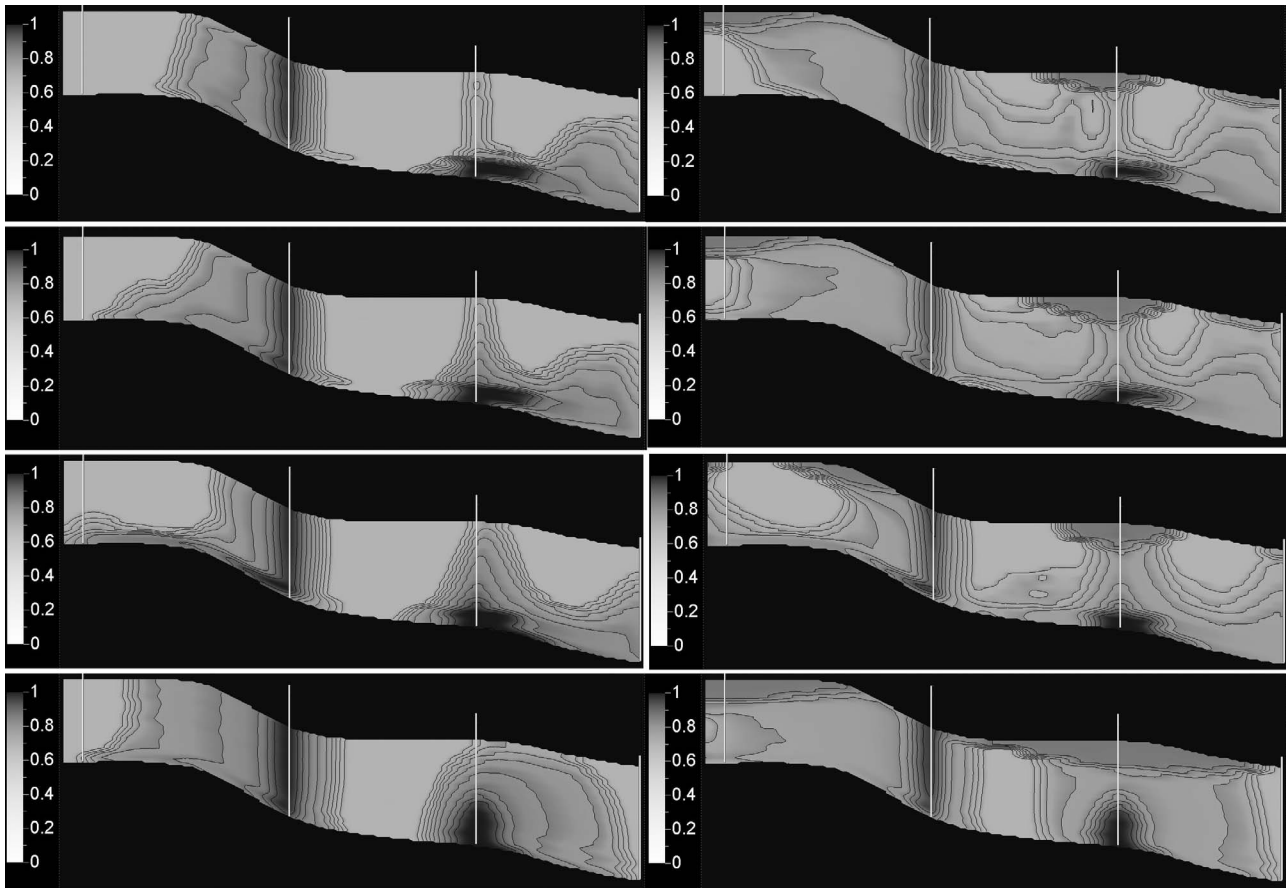
Figure 12. BC 4, open-with-brine, with two injectors and two producers. Gas-phase CO_2 saturation. (left) End of injection (50 years) and (right) end of monitoring. First row is FHRM; second row is facies model; third row is layered model; fourth row is formation model.

connectivity, two injectors and two producers were sited in the model (Figure 11 and Figure 12). The injectors are located in the central region, while the producers are located near the north and south boundaries. The producers are inactivated in BC 3 runs. Over a period of 50 years, CO_2 is injected at each well at 5 times the previous target rate, followed by 3050 years of monitoring, for the same total simulation time of 3100 years. Over the 50-year injection period, BC 3 runs achieved an average injection rate of 11 Mt/year, while BC 4 runs achieved an average rate of 17 Mt/year. The largest coal-fired power plant near Shute Creek, the Jim Bridger plant, produces CO_2 at approximately 18.5 Mt/year [*Allis et al.*, 2003]. Given the current boundary condition uncertainty and BHP constraint, sequestration of this much CO_2 will require two injection wells, with brine production needed if the reservoir is compartmentalized.

[60] In BC 3, without brine production, gas plume appears to be viscous dominated during injection, while gravity becomes important postinjection (Figure 11). Similar to the previous observation (Figure 8), the facies model is the most accurate while the layered model predicts incorrect physics during postinjection when viscous force is reduced. In BC 4, the producers extract brine from both ends of the model (Figure 12), inducing a different flow pattern from those previously simulated under the same BC (Figure 9). However, despite the changing flow pattern, the layered model has predicted the correct postinjection gravity override, likely due

to the enhanced viscous flow. Again, brine production acts to reduce the variability in the predictions made by the simple models. This result appears to be independent of the well design and the time scale of injection.

[61] In this study, pure CO_2 is injected into the reservoir. Given the formation temperature and pressure condition, fluid mobility ratio is fixed. No sensitivity study is conducted by varying the fluid composition. However, mobility effect can also affect model complexity. For example, by improving the mobility between the displacing and displaced phases (e.g., injecting CO_2 mixed with brine [*Qi et al.*, 2009]), the importance of detailed heterogeneity on model predictions could be reduced, i.e., the upscaled models become more accurate. If, however, the mobility ratio is made to be unfavorable (e.g., injecting CO_2 to displace heavy oil), the effect of detailed heterogeneity may become more important, thus performance of the upscaled models may degrade [*Kumar et al.*, 2005]. This is another reason why results of the present study are difficult to generalize.

[62] Although brine production is shown to be unimportant for pressure control if the reservoir is "open," that this result is obtained from modeling an infinitely large external aquifer, which may not be realistic even though the Nugget formation occurs at the regional scale. In reality, pressure pulse from injection will eventually reach an aquifer boundary or sealing fault. Thus boundary conditions simulated here represent end-member scenarios. Before injecting CO_2 at Shute Creek,

well tests of adequate durations are needed to detect and analyze the boundary, i.e., to determine the extent of reservoir compartment or distance to faults. These data, along with pressure and plume monitoring during the injection and closure phases, can be used to help refine the boundary condition assigned to the current models.

[63] Finally, in the storage schemes utilizing brine production, a large volume of brine can be produced and must be disposed of. Potential options for brine disposal include desalinization, beneficial use of the treated water, and disposal of residual high-density brine via reinjection [*Surdam et al.*, 2008]. However, brine treatment and reinjection are expensive, future work will seek means to optimize the entire operation, thereby both enhancing storage security and reducing cost.

5. Conclusions

[64] In this study, model complexity is evaluated by developing multiple conceptual models for the Nugget Sandstone, a deep saline aquifer in western Wyoming. A fully heterogeneous reservoir model (FHRM) is first built, where each grid cell is identified by multiple material tags (e.g., facies identification). On the basis of these tags, permeability upscaling is conducted to create three increasingly simpler models, a facies model (four units), a layered model (three units), and a formation model (one unit). The accuracy of upscaling is evaluated by conducting single-phase verification tests in the upscaled models, with the FHRM providing reference predictions. Then, large-scale CO_2 storage simulation is conducted in all models to assess the effect of conceptual model uncertainty on predicting CO_2 flow and storage. At the injection site, since uncertainty exists in the characteristics of the reservoir compartment, end-member boundary conditions are evaluated, whereby brine production is introduced to control formation fluid pressure. The effect of conceptual model uncertainty on model prediction is assessed for each boundary condition, with results elucidating the interplays between fluid driving force, heterogeneity resolution, and boundary condition.

[65] Results suggest that equivalent permeabilities obtained for the upscaled models are stable values independent of the flow configurations used in upscaling. In CO_2 modeling, for the spatial and temporal scales considered, without brine production, optimal complexity of the upscaled model depends on the prediction metric of interest; the facies model is the most accurate at capturing plume shape, fluid pressure, and CO_2 mass profiles, while the formation model is adequate for pressure prediction. The layered model is not accurate for predicting most of the performance metrics. Moreover, boundary condition impacts fluid pressure and the amount of CO_2 that can be injected. For the boundary conditions tested, brine production can modulate fluid pressure, affect the direction of mobile gas flow, and influence the accuracy of the upscaled models. In particular, the importance of detailed geologic resolution is weakened when viscous force is strengthened in relation to gravity force. When brine production is active, variability of the predictions by the upscaled models becomes smaller and the predictions are more accurate.

[66] The method of this study is applicable to the study of other systems. Here, under the scenarios tested, an upscaled model with adequate geological resolution is found to capture important prediction metrics of the heterogeneous model. This points to the possibility that simple models can be useful for CO_2 storage simulation, rather than striving for the most complex and costly model. However, simulation results here are only relevant to cases where a uniform relative permeability prevails in the storage reservoir, which may not be realistic given the magnitude of variation of the intrinsic permeability. Future work will address upscaling of relative permeabilities where multiple, facies-based relative permeability families can be assigned to the FHRM and suitable effective functions sought for the upscaled models. Further, though the facies model is identified as an optimal model (under brine production, perhaps the formation model), in practice, equivalent permeability is not easily obtainable. Future work will develop calibration strategy to obtain inverse permeabilities for the upscaled models that are consistent with the equivalent values.

[67] FHRM of this study was upscaled from a fine-grid geostatistical model for computation efficiency. Future work will directly model the fine gird using high-performance computing. With higher speed, a comprehensive uncertainty analysis can be conducted. For example, in creating the geostatistical model, uncertainties that have not been evaluated include k_V/k_H, geostatistical parameters in facies and ϕ modeling, and $\phi - \log(k)$ transforms. These uncertainties pertain to how accurately the FHRM represents the site condition, which will be relevant when the goal of the simulation is to predict the actual performance during CO_2 injection. However, site-specific analysis can only capture uncertainty at a single location. To further test insights of this study, future work should address reservoirs at different depth, T/P regime, fluid types, permeability structure, heterogeneity variance, etc. Experience with these systems will lead to insights that can be more readily generalized.

References

Allis, R., T. Chidsey, C. Morgan, J. Moore, and S. White (2003), CO_2 sequestration potential beneath large power plants in Colorado plateau-southern Rocky Mountain region, USA, paper presented at Second Annual Conference on Carbon Sequestration, Dep. of Energy, Alexandria, Va.

Amaziane, B., A. Bourgeat, and J. Koebbe (1991), Numerical simulation and homogenization of two-phase flow in heterogeneous porous media, *Transp. Porous Media*, 6, 519–547.

Ataie-Ashtiani, B., S. M. Hassanizadeh, and M. A. Celia (2002), Effects of heterogeneities on capillary pressure-saturation-relative permeability relationships, *J. Contam. Hydrol.*, 56, 175–192.

Bennion, B., and S. Bachu (2005), Relative permeability characteristics for supercritical CO_2 displacing water in a variety of potential sequestration zones in the western Canada sedimentary basin, *Rep. SPE 95547*, Soc. of Petrol. Eng., Richardson, Tex.

Bennion, B., and S. Bachu (2006a), The impact of interfacial tension and pore-size distribution/capillary pressure character on CO_2 relative permeability at reservoir conditions in CO_2-brine systems, *Rep. SPE 99325*, Soc. of Petrol. Eng., Richardson, Tex.

Bennion, B., and S. Bachu (2006b), Supercritical CO_2 and H_2S-brine drainage and imbibitions relative permeability relationships for intergranular sandstone and carbonate formations, *Rep. SPE 99326*, Soc. of Petrol. Eng., Richardson, Tex.

Birkholzer, J. T., and Q. Zhou (2009), Basin-scale hydrogeologic impacts of CO_2 storage: Capacity and regulatory implications, *Int. J. Greenhouse Gas Control*, *3*, 745–756.

Birkholzer, J. T., Q. Zhou, and C.-F. Tsang (2009), Large-scale impact of CO_2 storage in deep saline aquifers: A sensitivity study on pressure response in stratified systems, *Int. J. Greenhouse Gas Control*, *3*, 181–194.

Braun, C., R. Helmig, and S. Manthey (2005), Macro-scale effective constitutive relationships for two-phase flow processes in heterogeneous porous media with emphasis on the relative permeability-saturation relationships, *J. Contam. Hydrol.*, *76*, 47–85.

Carey, B., C. Christopher, and J. Gale (2007), Overview of the IEA Greenhouse Gas R&D Programme's Wellbore Integrity Network, paper presented at Technical Workshop on Geosequestration: Well Construction and Mechanical Integrity Testing, Environ. Prot. Agency, Los Alamos, N. M. (Available at http://www.epa.gov/ogwdw000/uic/pdfs/page_uic_albuquerque_presentations.pdf.)

Carlson, F. (1981), Simulation of relative pearmeability hysteresis to the non-wetting phase, *Rep. SPE 10157*, Soc. of Petrol. Eng., Richardson, Tex.

Castellini, A., A. Chawathe, D. Larue, J. Landa, F. Jian, J. Toldi, and M. Chien (2003), What is relevant to flow? A comprehensive study using a shallow marine reservoir, *Rep. SPE 79669*, Soc. of Petrol. Eng., Richardson, Tex.

Coburn, T. C., P. Corbett, A. Datta-Gupta, J. Jensen, M. Kelkar, D. Oliver, and C. D. White (2006), A virtual conversation on the impact of geostatistics in petroleum, production, and reservoir engineering, *AAPG Comput. Appl. Geol.*, *5*, 23–33.

Das, D. B., S. M. Hassanizadeh, and B. E. Rotter (2004), A numerical study of micor-heterogeneity effects on upscaled properties of two-phase flow in porous media, *Transp. Porous Media*, *56*, 329–350.

Doughty, C., and K. Pruess (2004), Modeling supercritical carbon dioxide injection in heterogeneous porous media, *Vadoes Zone J.*, *3*, 837–847.

Eaton, B. (1969), Fracture gradient prediction and its application in oilfield operations., *J. Petrol. Technol.*, *42*, 1353–1360.

Elfenbein, C., P. Ringrose, and M. Christie (2005), Small-scale reservoir modeling tool optimizes recovery offshore norway, *J. World Oil*, *226*, 45–59.

Ertekin, T., J. Abou-Kassem, and G. R. King (2001), *Basic Applied Reservoir Simulation*, Soc. of Petrol. Eng., Richardson, Tex.

Flett, M., R. Gurton, and I. Taggart (2004), The function of gas-water relative permeability hysteresis in the sequestration of carbon dioxide in saline formations, *Rep. SPE 88485*, Soc. of Petrol. Eng., Richardson, Tex.

Flett, M., R. Gurton, and G. Weir (2007), Heterogeneous saline formations for carbon dioxide disposal: Impact of varying heterogeneity on containment and trapping, *J. Petrol. Sci. Eng.*, *57*, 106–118, doi:10.1016/j.petrol.2006.08.016.

Flett, M., et al. (2008), Gorgon project: Subsurface evaluation of carbon dioxide disposal under barrows island, *Rep. SPE 116372*, Soc. of Petrol. Eng., Richardson, Tex.

Friedmann, F., A. Chawathe, and D. Larue (2003), Assessing uncertainty in channelized reservoirs using experimental designs, *Rep. SPE 85117*, Soc. of Petrol. Eng., Richardson, Tex.

Hesse, M., H. Tchelepi, and F. J. Orr (2006), Scaling analysis of the migration of CO_2 in saline aquifers, *Rep. SPE 102796*, Soc. of Petrol. Eng., Richardson, Tex.

Holloway, S., A. Chadwick, E. Lindeberg, I. Czernichowski-Lauriol, and R. Arts (2004), Best practice manual from Saline Aquifer CO_2 Storage Project, Statoil, Strondheim, Norway. (Available at http://www.co2store.org/TEK/FOT/SVG03178.nsf/Attachments/SACSBestPractiseManual.pdf/FILE/SACSBestPractiseManual.pdf.)

Ide, S., K. Jessen, and F. J. Orr (2007), Storage of CO_2 in saline aquifers: Effects of gravity, viscous, and capillary forces on amount and timing of trapping, *Int. J. Greenhouse Gas Control*, *1*, 481–491.

Intergovernmental Panel on Climate Change (2005), Special report on carbon dioxide capture and storage, Geneva. (Available at http://arch.rivm.nl/env/int/ipcc/pagesmedia/SRCCSfinal/IPCCSpecialReportonCarbondioxide-CaptureandStorage.htm.)

Johnson, J., J. Nitao, C. I. Steefel, and K. Knauss (2001), Reactive transport modeling of geologic CO_2 sequestration in saline aquifers: The influence of intra-aquifer shales and the relative effectiveness of structural, solubility, and mineral trapping during prograde and retrograde sequestration, Lawrence Livermore Natl. Lab., Livermore, Calif. (Available at http://www.netl.doe.gov/publications/proceedings/01/carbonseq/P28.pdf.)

Juanes, R., E. Spiteri, F. J. Orr, and M. Blunt (2006), Impact of relative permeability hysteresis on geological CO_2 storage, *Water Resour. Res.*, *42* W12418, doi:10.1029/2005WR004806.

Kumar, A., M. Noh, G. Pope, K. Sepehrnoori, S. Bryant, and L. Lake (2004), Reservoir simulation of CO_2 storage in deep saline aquifers, *Rep. SPE 89343*, Soc. of Petrol. Eng., Richardson, Tex.

Kumar, M., V. Hoang, C. Satik, and D. H. Rojas (2005), High mobility ratio water flood performance prediction: Challenges and new insights, *Rep. SPE 97671*, Soc. of Petrol. Eng., Richardson, Tex.

Law, D., and S. Bachu (1996), Hydrogeological and numerical analysis of CO_2 disposal in deep aquifers in the Alberta sedimentary basin, *Energy Convers. Manage.*, *37*, 1167–1174.

Li, S. Q., Y. Zhang, X. Zhang, and C. G. Du (2011), Geological modeling and fluid flow simulation of acid gas disposal in western Wyoming, *AAPG Bull.*, in press.

Lindquist, S. (1988), Practical characterization of eolian reservoirs for development: Nugget sandstone, Utah-Wyoming thrust belt, *J. Sediment. Geol.*, *56*, 315–339.

Maldal, T., and I. Tappel (2004), CO_2 underground storage for snohvit gas field development, *Energy*, *29*, 1403–1411, doi:10.1016/j.energy.2004.03.074.

McPherson, B., and B. Cole (2000), Multiphase CO_2 flow, transport and sequestration in the Powder River Basin, Wyoming, U.S.A, *J. Geochem. Explor.*, *69*, 65–69.

Michael, K., G. Allinson, A. Golab, S. Sharma, and V. Shulakova (2009a), CO_2 storage in saline aquifers, II, Experience from existing storage operations, *Energy Proc.*, *1*, 1973–1980.

Michael, K., M. Arnot, P. Cook, J. Ennis-King, R. Funnell, J. Kaldi, D. Kirste, and L. Paterson (2009b), CO_2 storage in saline aquifers, I, Current state of scientific knowledge, *Energy Proc.*, *1*, 3197–3204.

Michael, K., A. Golab, V. Shulakova, J. Ennis-King, G. Allinson, S. Sharma, and T. Aiken (2010), Geological storage of CO_2 in saline aquifers—A review of the experience from existing storage operations, *Int. J. Greenhouse Gas Control*, *4*, 659–667.

Milliken, W., M. Levy, S. Strebelle, and Y. Zhang (2007), The effect of geologic parameters and uncertainties on subsurface flow: Deepwater depositional systems, *Rep. SPE 109950*, Soc. of Petrol. Eng., Richardson, Tex.

Nordbotten, J., M. Celia, and S. Bachu (2005), Injection and storage of CO_2 in deep saline aquifers: Analytical solution for CO_2 plume evolution during injection, *Trans. Porous Media*, *58*, 339–360, doi:10.1007/s11242-004-0670-9.

Obi, E., and M. Blunt (2006), Streamline-based simulation of carbon dioxide storage in a north sea aquifer, *Water Resour. Res.*, *42*, W03414, doi:10.1029/2004WR003347.

Orr, F. M. (2009), Onshore geological storage of CO_2, *Science*, *325*, 1656–1658.

Pickup, G., K. Stephen, J. Ma, P. Zhang, and J. Clark (2005), Multi-stage upscaling: Selection of suitable methods, *Trans. Porous Media*, *58*, 191–216.

Primera, A., W. Sifuentes, and N. Rodriguez (2009), CO_2 injection and storage: A new approach using integrated asset modeling, *Rep. SPE 121970*, Soc. of Petrol. Eng., Richardson, Tex.

Pruess, K., J. Garcia, T. Kovscek, C. Oldenburg, J. Rutqvist, C. Steefel, and T. Xu (2004), Code intercomparison builds confidence in numerical simulation models for geologic disposal of CO_2, *Energy*, *29*, 1431–1444, doi:10.1016/j.energy.2004.03.077.

Qi, R., T. LaForce, and M. Blunt (2007), Design of carbon dioxide storage in a North Sea aquifer using streamline-based simulation, *Rep. SPE 109905*, Soc. of Petrol. Eng., Richardson, Tex.

Qi, R., T. LaForce, and M. Blunt (2009), Design of carbon dioxide storage in aquifers, *Int. J. Greenhouse Gas Control*, *3*, 195–205.

Renard, P., and G. de Marsily (1997), Calculating equivalent permeability: A review, *Adv. Water Resour.*, *20*, 253–278.

Sáez, A. E., C. J. Otero, and I. Rusinek (1989), The effective homogeneous behavior of heterogeneous porous media, *Trans. Porous Media*, *4*, 213–238.

Sanchez-Vila, X., A. Guadagnini, and J. Carrera (2006), Representative hydraulic conductivities in saturated groundwater flow, *Rev. Geophys.*, *44*, RG3002, doi:10.1029/2005RG000169.

Sasaki, K., T. Fujii, Y. Niibori, T. Ito, and T. Hashida (2008), Numerical simulation of supercritical CO_2 injection into subsurface rock masses, *Energy Conversion Manage.*, *49*, 54–61, doi:10.1016/j.enconman.2007.05.015.

Schlumberger (2009), Eclipse technical description manual, Abingdon, U. K.

Stauffer, P., H. Viswanathan, R. Pawar, and G. Guthrie (2009), A system model for geologic sequestration of carbon dioxide, *Environ. Sci. Technol.*, *43*, 565–570.

Surdam, R. C., K. Clarey, R. D. Bentley, S. J. E., and Z. Jiao (2008), Desalinization project feasibility, in *Water Associated with Coal Beds in Wyoming's Powder River Basin*, *Explor. Mem.*, vol. 2, edited by D. A. Copeland and M. L. Ewald, pp. 295–311, Wyo. State Geol. Surv., Laramie, Wyo.

Surdam, R. C., Z. Jiao, P. Stauffer, and T. Miller (2009), *An Integrated Strategy for Carbon Management Combining Geological CO_2 Sequestration, Displacement Fluid Production, and Water Treatment, Challenges in Geol. Resour. Dev.*, vol. 8, Wyo. State Geol. Surv., Laramie, Wyo.

Wen, X.-H., and J. Gomez-Hernandez (1996), Upscaling hydraulic conductivities in heterogeneous media: An overview, *J. Hydrol.*, *183*, ix–xxxii.

Wen, X.-H., L. Durlofsky, and M. Edwards (2003), Use of border regions for improved permeability upscaling, *Math. Geol.*, *35*, 521–547.

Wolery, T. J., R. Aines, Y. Hao, W. Bourcier, T. Wolfe, and C. Haussman (2009), Fresh water generation from aquifer pressured carbon storage: Annual report FY09, *Rep. lLNL-TR-420857*, Lawrence Livermore Natl. Lab., Livermore, Calif.

Zhang, Y., and C. W. Gable (2008), Two-scale modeling of solute transport in an experimental stratigraphy, *J. Hydrol.*, *348*, 395–411, doi:10.1016/j.jhydrol.2007.10.017.

Zhang, Y., C. W. Gable, and M. Person (2006), Equivalent hydraulic conductivity of an experimental stratigraphy - Implications for basin-scale flow simulations, *Water Resour. Res.*, *42*, W05404, doi:10.1029/2005WR004720.

Zhang, Y., B. Liu, and C. Gable (2011), Three-dimensional hydraulic conductivity upscaling for hierarchical sedimentary deposits at multiple scales based on a synthetic aquifer, *Transp. Porous Media*, *87*(3), 717–737, doi:10.1007/s11242-010-9711-8.

Zhou, Q., J. Birkholzer, T. C. F., and J. Rutqvist (2008), A method for quick assessment of CO_2 storage capacity in closed and semi-closed saline formations, *Int. J. Greenhouse Gas Control*, *2*, 626–639.

Zhou, Q., J. T. Birkholzer, E. Mehnert, Y.-F. Lin, and K. Zhang (2010), Modeling basin- and plume-scale processes of CO_2 storage for full-scale deployment, *Ground Water*, *48*, 494–514.

S. Li and Y. Zhang, Department of Geology and Geophysics, University of Wyoming, 1000 E. University Ave., Laramie, WY 82071, USA. (sli2@uwyo.edu; yzhang9@uwyo.edu)

X. Zhang, Schlumberger Information Solutions, Schlumberger, 5599 San Felipe, Suite 1700, Houston, TX 77056, USA.